Published in final edited form as:
Curr Mol Med. 2013 December ; 13(10): 1613–1632.

Functionalized Upconversion Nanoparticles: Versatile Nanoplatforms for Translational Research

Feng Chen[1], **Wenbo Bu**[*,1], **Weibo Cai**[2], and **Jianlin Shi**[*,1]

[1] State Key Laboratory of High Performance Ceramics and Superfine Microstructure, Shanghai Institute of Ceramics, Chinese Academy of Sciences, Shanghai, 200050, People's Republic of China

[2] Departments of Radiology and Medical Physics, University of Wisconsin - Madison, Wisconsin, United States

Abstract

The design, application, and translation of targeted multimodality molecular imaging probes based on nanotechnology has attracted increasing attentions during the last decade and will continue to play vital roles in cancer diagnosis and personalized medicine. With the growing awareness of drawbacks of traditional organic dyes and quantum dots, biocompatible lanthanide ion doped upconversion nanoparticles have emerged as promising candidates for clinically translatable imaging probes, owing to their unique features that are suitable for future targeted multimodal imaging in living subjects. In this review, we summarized the recent advances in the field of functionalized upconversion nanoparticles (f-UCNP) for biological imaging and therapy *in vivo*, and discussed the future research directions, obstacles ahead, and the potential use of f-UCNP in translational research.

Keywords

Molecular Imaging; Multimodality Probe; Personalized Therapy; Translational Research; Upconversion Nanoparticle (UCNP)

INTRODUCTION

Cancer nanotechnology is an emerging interdisciplinary research field, which holds great potential for enabling the design and fabrication of future multifunctional nano-systems to boost both targeted molecular imaging and personalized therapies [1-3]. The term “molecular imaging” is defined as the visual representation, characterization, and quantification of biological processes at the cellular and subcellular levels within intact living organisms [4]. Molecular imaging allows sensitive and specific monitoring of key molecular targets and host responses associated with various biological events using single or combined imaging modalities, such as positron emission tomography (PET) [5-7], single-photon emission computed tomography (SPECT) [8, 9], molecular magnetic resonance imaging (MRI), magnetic resonance spectroscopy (MRS), optical bioluminescence , optical fluorescence [10, 11], and targeted ultrasound [4]. The design, application, and translation of targeted multimodality molecular imaging probes based on nanotechnology has attracted increasing attentions during the last decade and will continue to play vital roles in cancer

[*]**Corresponding authors:** Prof. Jianlin Shi & Prof. Wenbo Bu State Key Laboratory of High Performance Ceramics and Superfine Microstructure, Shanghai Institute of Ceramics, Chinese Academy of Sciences, Shanghai, 200050, People's Republic of China jlshi@sunm.shcnc.ac.cn & wbbu@mail.sic.ac.cn Tel.: 86-21-52412712 &86-21-52412610 Fax: 86-21-52412122.

staging, evaluating the presence or absence of metastases, tailoring individualized therapies, monitoring the treatment response, studying the pharmacokinetics in clinical and pre-clinical settings, decreasing the workload and facilitating the translation of promising diagnostic and therapeutic technologies from bench to bedside [4, 12-15].

In the pool of available nanoplatforms for designing suitable diagnosis and therapy integrated nanosystems [16-32], lanthanide ion doped upconversion nanoparticles (UCNPs) have emerged as promising candidates for molecular imaging applications, due to their unique features that are highly suitable for targeted multimodal imaging in living subjects [33]. First, upconversion luminescence (UCL) is a unique process where low energy continuous-wave (CW) of near-infrared (NIR) light is converted to higher energy light through the sequential absorption of multiple photons or energy transfer [34], which exhibits attractive optical features such as sharp emission lines [35, 36], long lifetimes (~ms) [37], large anti-Stokes shift [35], superior photo-stability [38], high detection sensitivity [39], non-blinking and non-bleaching [38, 40], high tissue penetration depth [41], minimal photo-damage[42] and lack of autofluorescence [43, 44]. Second, with the doping of well-selected lanthanide ions of Gd^{3+}, Er^{3+}/Yb^{3+} and Tm^{3+}/Yb^{3+} (or combination of these ions), MRI and multicolor UCL imaging (emission bands ranging from ultraviolet [UV] to NIR region) could be readily achieved [45-48]. Third, in comparison with traditional organic dyes and quantum dots (QDs), UCNP excludes the potential UV photo-damage and has been demonstrated to be much more biocompatible with extremely low toxicity in living systems [49, 50]. Fourth, core@multi-shell structured UCNP is inherently a UCL/MRI/CT (i.e. computed tomography) tri-modal imaging nanoplatform [46, 51], which can be further functionalized with polymer coating such as poly(ethylene glycol) (PEG) for prolonged blood circulation lifetime and stealth capabilities, radioisotopes such as ^{64}Cu for PET imaging, cleavable anticancer drugs (or genes) for controlled drug release and cancer therapy, single or combined targeting ligands for targeted visualization of diseases *in vivo*. With these desirable features, functionalized upconversion nanoparticles (denoted as f-UCNP) can serve as versatile nanoplatforms for future cancer-targeted multimodal imaging and controllable therapy (***Scheme 1***).

To address the future research directions, obstacles ahead, and the potential use of f-UCNP for translational research, in this review article we summarized the recent advances regarding the use of f-UCNP in biological imaging and therapy *in vivo* (Table 1). The techniques for the synthesis of UCNP will be briefly described, with a focus on the challenges in fabricating sub-10 nm sized high quality UCNP. In particular, the use of Gd^{3+} doped UCNP as a novel nanoplatform for building multifunctional UCNP-based diagnostic (or therapeutic) agents will be discussed. We will also describe the few successful examples of *in vivo* targeted tumor imaging with UCNP. In addition, the biodistribution and *in vivo* biological interaction of water soluble UCNP will be reviewed in detail. Importantly, the challenges, such as the short blood circulation time, rapid reticuloendothelial system (RES) accumulation, extremely slow clearance rate, imperfect targeting strategies (or efficiency), among others will be discussed and potential solutions to these problems will also be illustrated. Lastly, we will also review the new applications of using f-UCNP for long term particle tracking *in vitro*, as well as the active development of NIR light triggered drug delivery systems based on UCNP.

SYNTHESIS OF MONODISPERSE OLEATE CAPPED UCNP

The most popular UCNPs for biological labeling and imaging are Er^{3+}/Yb^{3+} and Tm^{3+}/Yb^{3+} co-doped hexagonal $NaYF_4$ which display UV, blue green, red, and NIR emissions [33, 52, 53]. A number of synthetic techniques have recently been developed to enable the production of highly monodisperse UCNP with rationally designed geometries [54-59].

Oleic acid-assisted hydrothermal reaction and thermal decomposition are two of the most popular methods for the synthesis of monodisperse hydrophobic oleate capped UCNP [54, 56, 59]. For a comprehensive review on UCNP synthesis, shape, size and phase control, and surface modifications, the readers are referred to two excellent review articles [33, 53].

Recently, a modified method for high quality hexagonal-phase UCNP was developed which may represent the most adopted strategy for not only single core but also core@multi-shell UCNPs (***Fig. (1)***) [55]. With the doping of different lanthanide ion combinations (e.g. Er^{3+}/Yb^{3+} and Tm^{3+}/Yb^{3+}) in the separated crystal layers and surface protective coating which reduced the crystal defects [60], multicolored and tunable UCL property could be achieved [46, 61]. Although UCNP with various morphologies and tunable crystal sizes (from sub-50 nm to sub-micrometers) could be easily prepared with high reproducibility in different labs [54-57, 59], the combination of ultra-small particle size (sub-10 nm) and enhanced optical efficiency in one single UCNP remains a challenge.

SUB-10 NANOMETER SIZED UCNP: OPPORTUNITIES AND CHALLENGES

Technically, it is easy to synthesize ultra-small sized UCNP with particle diameter less than 10 nm by careful control of synthetic parameters, such as reaction temperature and time [58, 62, 63]. The challenge lies in how to reduce the increased surface defects, when decreasing the particle size, in order to preserve the UCL properties. Core@shell structured UCNP has been demonstrated to be one of the most effective strategies for reducing the surface defects to avoid the surface quenching effect [60]. However, the synthesis of sub-10 nm sized core@shell structured UCNP has not been reported to date, possibly due to the difficulty in excluding the homogeneous nucleation of the second protective layer.

The situation changes after the discovery of the magic role of Gd^{3+} when doped into the $NaYF_4$ matrix [58]. For the first time, it was demonstrated theoretically and experimentally that doping $NaYF_4$:Er^{3+}/Yb^{3+} with precisely defined Gd^{3+} ion concentrations could simultaneously allow precise control over the phase (from cubic to hexagonal), size (down to sub-10 nm) and UCL efficiency [58]. Successful synthesis of sub-10 nm sized high quality hexagonal-phase $NaYF_4$:Er^{3+}/Yb^{3+}/Gd^{3+} has been achieved using modified thermal decomposition method with Gd^{3+} doping fixed at 30 mol % and reaction temperature set down to 230 °C [58]. Subsequently, it was found that excessively increasing the Gd^{3+}-doping level may not be helpful, which could lead to decreased optical intensity due to the increase in surface defects caused by over-reduction of the particle size.

Li and co-workers solved this problem by replacing Y^{3+} with Lu^{3+}, and demonstrated a greatly enhanced UCL property in a ~8 nm sized β-$NaLuF_4$:Gd^{3+}/Yb^{3+}/Tm^{3+} nanocrystal (***Fig. (2A)***) [41]. In this report, oleylamine was used as both the surfactant and solvent, with Gd^{3+} doping at a 24% molar ratio. One disadvantage of this approach was the use of trifluoroacetate as the precursor, which might cause certain safety concerns during synthesis but could be solved by using a previously reported modified method [57]. As-synthesized sub-10 nm β-$NaLuF_4$:Gd^{3+}/Yb^{3+}/Tm^{3+}(24/20/1 mol %) nanocrystals displayed bright UCL with a quantum yield (QY) of 0.47±0.06%, which is higher than the previously reported 100 nm sized $NaYF_4$:Er^{3+}/Yb^{3+} (QY of 0.3±0.1%) [64]. The enhanced UCL was attributed to the presence of hexagonal phase and successful suppression of non-radiative processes by replacing β-$NaYF_4$ with β-$NaLuF_4$. Studies of citric acid modified β-$NaLuF_4$:Gd^{3+}/Yb^{3+}/Tm^{3+} in black mouse (***Fig. (2B)***) suggested a nearly 20 mm of penetration depth, which is among the best reported to date. Furthermore, the study also showed successful detection of < 50 β-$NaLuF_4$:Gd^{3+}/Yb^{3+}/Tm^{3+}-labeled cells after subcutaneous injection in nude mouse (***Fig. (2C)***), indicating that Gd^{3+}-doped β-$NaLuF_4$ can be a highly sensitive probe for future cell labeling/tracking *in vivo*. Another application of sub-10 nm sized UCNP lies in its

potential for the design of tumor targeted and renal clearable multimodal imaging probe. However, it is quite challenging to develop such a probe with hydrodynamic diameter (HD) below 5.5 nm, the renal cut off of nanoparticles *in vivo* [65].

Apart from greatly enhanced UCL properties, an additional advantage of Gd^{3+}-doped β-$NaLuF_4$ comes from the doping of paramagnetic Gd^{3+} ions, which can be used for MRI [45]. However, due to the lack of understanding on the role of surface and bulk Gd^{3+} ions in shortening the relaxation time of water protons and the related MRI relaxivity mechanisms, the first reported longitudinal relaxivity (r_1) of Gd^{3+}-doped UCNP was only 0.14 $mM^{-1}s^{-1}$/Gd^{3+}, which is significantly lower than that of clinically used gadolinium chelates (e.g. r_1 =3.8 $mM^{-1}s^{-1}$ for Gd-DTPA) and underscored the need for mechanism probing and sensitivity optimization.

MULTIMODALITY IMAGING PROBES BASED ON Gd^{3+} DOPED UCNP

Sensitivity Optimization of Gd^{3+} Doped UCNP

Since the dominant MRI sensitive ions in UCNP are Gd^{3+} ions, the MRI relaxivity can be improved by designing a $NaGdF_4$ layer to introduce more paramagnetic centers. Core@shell structured UCNPs with $NaGdF_4$ as the outermost shell have been reported, with the first example being PEG-phospholipid coated cubic phase $NaGdF_4$:Er^{3+}/Yb^{3+}@$NaGdF_4$ core@shell structured UCNP [40]. Relaxivity study on a 1.5 T MRI scanner showed r_1 relaxivities of 1.40 and 1.05 $mM^{-1}s^{-1}$ for 20 and 41 nm sized $NaGdF_4$:Er^{3+}/Yb^{3+}@$NaGdF_4$, respectively. A similar approach was later reported by replacing $NaGdF_4$:Er^{3+}/Yb^{3+} with Gd-free $NaYF_4$:Er^{3+}/Yb^{3+}, resulting in $NaYF_4$:Er^{3+}/Yb^{3+}@$NaGdF_4$ (the $NaGdF_4$ thickness was over 6 nm) [66]. In this study, the re-designed UCNP was coated with a dense silica shell and exhibited a r_1 relaxivity of 0.48 $mM^{-1}s^{-1}$, 3-fold higher than the first reported value (r_1=0.14 $mM^{-1}s^{-1}$) [45] but several fold lower than that of $NaGdF_4$:Er/Yb@$NaGdF_4$@PEG (r_1=1.4 $mM^{-1}s^{-1}$) [40]. Without complete understanding of the role of bulk and surface Gd^{3+} ion in shortening the T_1-time of water protons, these two reports might not have designed the core@shell structure properly to maximize r_1 relaxivity, either by using Gd-containing core or by growing an over-thick $NaGdF_4$ outer shell [40, 66].

Recently, we have designed Gd^{3+}-doped UCNPs with various Gd^{3+} ion locations and surface densities to probe the different roles of Gd^{3+} ions in UCNP on shortening the T_1-relaxation time of surrounding water molecules (***Fig. (3A)***) [46]. Hexagonal-phase $NaYF_4$:Er^{3+}/Yb^{3+}/Gd^{3+}(2/18/15 mol %) nanocrystal was chosen as the core (i.e. the first layer) and denoted as ***1st***. Epitaxial growth of the second (***2nd***: $NaYF_4$:Tm^{3+}/Yb^{3+}(0.3/25 mol %) and third layer (***3rd***: $NaGdF_4$) were achieved by a seed-mediated re-growth process, as demonstrated by size and shape evolutions in TEM images (***Fig. (3B)***). The formation of core@shell structure could also be confirmed by X-ray photoelectron spectroscopy (XPS) using synchrotron radiation [67]. However, determining the exact $NaGdF_4$ shell thickness or its distribution is very challenging and could only be roughly estimated through the use of various techniques such as scanning transmission electron microscopy image in the high-angle annular dark-field (STEM-HAADF) model, electron energy loss spectroscopy (EELS), and energy-dispersive X-ray spectroscopy (EDS) [68]. Water permeable dense silica shell has been used for transferring these UCNPs to aqueous solution before MRI relaxivity studies. Parallel r_1 relaxivity testing in a 3.0 T MRI suggested that only the surface Gd^{3+} ions in Gd^{3+}-doped UCNP are responsible for shortening the T_1-relaxation time of water protons. With the rigid lattice shielding effect in 1^{st}@2^{nd}@SiO_2, an almost completely “quenched” MRI enhanced signal was observed with its r_1 value estimated to be 0.037 $mM^{-1}s^{-1}$ (***Fig. (3C)***), 33.5-fold smaller than 1^{st}@SiO_2 with a similar silica shell thickness (~ 10 nm). Furthermore, a remarkable increase in r_1–relaxivity (from 2.18 to 6.18

$mM^{-1}s^{-1}$) was achieved by decreasing the $NaGdF_4$ shell thickness down to < 1 nm, which demonstrated the co-existence of positive (for UCL) and negative (for MRI) lattice shielding effects in $NaYF_4$:Er^{3+}/Yb^{3+}@$NaGdF_4$. By using ultra-small $NaGdF_4$ nanocrystals as models, Veggel and co-workers have shown the same observation of increased r_1-relaxivity per Gd^{3+} ion (from 3.0 to 7.2 $mM^{-1}s^{-1}$) with decreased $NaGdF_4$ particle size (from 8 to 2.5 nm), again demonstrating the role of surface Gd^{3+} ions in relaxivity enhancement [63].

Each imaging modality has its strengths and weaknesses [4, 69-72]. MRI provides excellent spatial resolution (several tens of micrometers), exceptional anatomical information and unlimited depth for *in vivo* imaging, but suffers from limited sensitivity. PET possesses a remarkable detection sensitivity reaching below picomolar range for functional imaging with a low spatial resolution (~mm). PET and MRI are unsuitable for imaging single living cells owing to the low planar resolution. Photoluminescence imaging is capable of providing the highest spatial resolution (several hundreds of nanometers) and is good at imaging live cells, however it lacks the capability to obtain anatomical and physiological detail *in vivo* because of limited penetration of light in tissues. To achieve a balance in sensitivity, resolution, and penetration depth when visualizing (cancer) cells from the cellular scale to non-invasive imaging, photoluminescence emission, radioactivity, and magnetic properties may be combined within one nanoplatform for satisfactory multiscale/multimodal imaging. The use of Gd^{3+} doped UCNP represents one promising approach to achieve this goal.

Combination of UCL with MRI

Gd^{3+} doped UCNP is a promising bimodal nanoplatform for UCL/MRI and future theranostic nanomedicine. When compared to organic dyes and QDs, UCNP has many advantages such as the absence of photo-damage to living organisms, low autofluorescence, high detection sensitivity, just to name a few [33, 35]. Furthermore, doping Tm^{3+} ions in UCNP can be even more advantageous because of the NIR-to-NIR upconversion process, which enables high contrast imaging in deeper tissues. After the first successful demonstration of *in vivo* imaging using Tm^{3+}/Yb^{3+} co-doped UCNP [73], many interesting UCNP-based nanostructures have been developed [74-81]. The first *in vivo* demonstration of bimodal UCL/MRI imaging was achieved using hexagonal-phase carboxylic acid-functionalized $NaGdF_4$:Tm^{3+}/Er^{3+}/Yb^{3+} nanoparticles [74]. After administration of the probe (dose: 1.5 mg/kg), fast and prominent uptake in the liver and spleen could be observed using a 3.0 T clinical MRI scanner (***Fig. (4A)***), which was confirmed by UCL imaging with a 980 nm laser excitation (***Fig. (4B)***). Much future effort needs to be directed towards MRI sensitivity optimization, surface modification, and *in vivo* targeting of these bimodal imaging probes.

UCNP as CT Contrast Agents

With the presence of heavy metal ions like Gd^{3+}, Yb^{3+}, and Lu^{3+} in $NaYF_4$ matrix, lanthanide ions doped UCNP also represents a new class of UCL/MRI/CT tri-modal contrast agent [51, 82-84], which can overcome the limitations (e.g. single modality, large dose needed, short circulation lifetime, lack of targeting capability, and potential renal toxicity) of traditional iodinated CT contrast agents [85, 86]. Such UCNP can be readily detected by three imaging modalities, with one single sub-20 nm sized nanoparticle with suitable lanthanide ions doping. $NaGdF_4$:Er^{3+}/Yb^{3+}, synthesized *via* an oleic acid/1–butyl-3-methylimidazolium tetrafl uoroborate two-phase system, was first reported as such a tri-modal contrast agent [82]. In a followed-up study, Yb-based $NaYbF_4$:Er^{3+}/Gd^{3+} nanocrystal was reported with even higher CT contrast effect (***Fig. (5A)***) [51]. One interesting aspect of this study was the doping of well-controlled amount of Gd^{3+} ions, which turned out to be highly useful for achieving small (~20 nm) and shape-controllable nanocrystals, in addition to improving the UCL property and rendering MRI sensitivity. As-synthesized water soluble

PEG-modified $NaYbF_4$:Er^{3+}/Gd^{3+} (PEG-UCNPs) was found to be the best CT contrast agents among iobitridol, Au-, Pt-, Bi-, and Ta-based nanoparticulate agents under the same conditions, where a clear enhancement of the signal from the heart was observed within 20 min after intravenous administration (***Fig. (5B&C)***). In addition, *in vivo* imaging demonstrations of the UCL and MRI properties and *in vivo* lymph node mapping were also achieved. Importantly, no toxic free Gd^{3+} ion leaching from the PEG-UCNPs was observed even after one week [51]. Short-term toxicity investigation revealed no tissue damage or other adverse effects in major organs at three weeks post-injection of PEG-UCNPs, although only 34% of the administrated probe could be cleared from the mice in 3 weeks. Long-term safety profile and possible elimination pathways of UCNP *in vivo* will need to be investigated in the future.

Radiolabeled UCNP for PET Imaging

The use of f-UCNP as UCL/MRI/CT tri-modal contrast agents is under active exploration. Radiolabeling of UCNP, which can add PET/SPECT sensitivity and facilitate future clinical translation, has been very rare. Recently, radiolabeled UCNP based on surface ion reaction between $^{18}F^-$ and rare-earth ions was reported (***Fig. (6)***) [87-90], where $^{18}F^-$ was incubated with nanoparticles containing rare-earth ions (e.g. Y_2O_3, $NaYF_4$, $NaYF_4$:Yb^{3+}/Tm^{3+}, $Y(OH)_3$ and $Gd(OH)_3$). Intriguingly, labeling of $^{18}F^-$ can be achieved with an average yield of > 90% in only one minute [89]. The optimal labeling conditions were found to be concentration- and incubation time-dependent, which may also vary between different nanoparticles. Control experiments using other nanoparticles that do not contain rare-earth ions ruled out the possible contribution from physical absorption, which suggested that such efficient and rapid ^{18}F-labeling was due to a specific inorganic reaction between $^{18}F^-$ and rare-earth ions. *In vivo* and e*x vivo* PET imaging revealed rapid accumulation of nanoparticles in the liver (~61.4% ID/g) and spleen (~45.2% ID/g) within 5 min, whereas uptake in the heart, lungs, kidney and other organs was quite low (< 10% ID/g). The relatively high stability of ^{18}F-labeling was confirmed by the very low radioactivity observed in the bone, as well as weak radioactive signal in the kidneys. Since Gd^{3+} ions could be easily introduced into the UCNP matrix, either by doping or surface cation exchange, T_1-weighted MRI was also carried out to provide anatomical information in the follow-up studies [88, 90]. Of note, the abovementioned rapid and efficient labeling of rare-earth nanoparticles with ^{18}F may not represent a general strategy for labeling other PET/SPECT isotopes such as ^{11}C ($t_{1/2}$: 20.4 min), ^{64}Cu ($t_{1/2}$: 12.7 h), ^{68}Ga ($t_{1/2}$: 67.7 min), ^{86}Y ($t_{1/2}$: 14.7 h), ^{89}Zr ($t_{1/2}$: 3.3 d), ^{124}I ($t_{1/2}$: 4.2 d), ^{99m}Tc ($t_{1/2}$: 6.0 h), ^{111}In ($t_{1/2}$: 2.8 d), etc. [91-97]. Considering the relatively short half-life of ^{18}F ($t_{1/2}$: 109.7 min) and the limited potential of radiolabeling through ion-reaction, much research remains to be done in the near future to optimize the radiolabeling, stability, and *in vivo* targeting capability of f-UCNP.

IN VIVO TUMOR TARGETING AND IMAGING WITH UCNP

In vitro targeted cellular imaging based on folic acid (FA)-conjugated [52, 98-100] and antibody-labeled UCNP [45, 101-104] has been well-documented, while *in vivo* targeted imaging using f-UCNP is still at its infancy [43, 105, 106]. Integrin $\alpha_v\beta_3$ plays a critical role in tumor angiogenesis, the formation of new blood vessels, and is a receptor for the extracellular matrix proteins with the exposed arginine-glycine-aspartic peptide (RGD) tri-peptide sequence [107]. Inspired by the great success in targeted imaging of tumor angiogenesis using various nanoparticles [16, 108], the first *in vivo* targeted imaging of UCNP ($NaYF_4$:Er^{3+}/Yb^{3+}/Tm^{3+}, ~14 nm) was also achieved using integrin $\alpha_v\beta_3$ as the target [43]. With the co-doping of Tm^{3+}/Yb^{3+} in UCNP, strong NIR emission could be achieved for good tissue penetration of signal. Using UCNP-RGD as the targeting probe, specific *in vitro* targeting was achieved in human glioblastoma U87MG cells (expressing

high level of integrin $\alpha_v\beta_3$) as compared to human breast cancer cell line MCF-7 (expressing low level of integrin $\alpha_v\beta_3$). In athymic nude mice bearing both U87MG and MCF-7 tumors, specific *in vivo* targeting of UCNP-RGD to the U87MG tumor was demonstrated with an excellent signal-to-noise ratio of ~24 (***Fig. (7)***), which was validated by *ex vivo* imaging and biodistribution studies of Y^{3+} ions in different organs [43].

Using FA- and neurotoxin-conjugated UCNP, targeted UCL imaging in tumor-bearing mice have also been demonstrated in follow-up studies [105, 106]. With the presence of larger surface areas for targeting ligand conjugation, novel tumor-specific antibody fragments, growth factors, peptides, and small molecules can be attached to UCNP for *in vivo* tumor targeting. Understanding the biodistribution profile, clearance pathways, as well as long term toxicity of f-UCNPs is vital for further investigating their targeting capability and potential clinical translation.

BIODISTRIBUTION, CLEARANCE, AND LONG TERM TOXICITY OF UCNP

Many *in vitro* studies have demonstrated relatively low toxicity of f-UCNP with various sizes, shapes and surface coatings [40, 41, 79, 80, 109]. Further understanding of the fate of f-UCNP in living subjects is very important. Similar to other nanoparticle-based imaging probes, the major concern of f-UCNP lies in the rapid RES uptake and relatively slow hepatic clearance in small animals [49, 51, 110]. In one study, the biodistribution, clearance, and long term toxicity of polyacrylic acid (PAA) coated $NaYF_4$:Tm^{3+}/Yb^{3+} (denoted as PAA-UCNP; ~11.5 nm) was investigated after intravenous injection into mice at a 15 mg/kg dose [49]. The biodistribution and clearance of PAA-UCNP was first qualitatively evaluated based on the UCL signal (***Fig. (8)***), and subsequently validated by quantitative measurement of Y^{3+} concentration in the organs by inductively coupled plasma atomic emission spectroscopy (ICP-AES) analysis. It was found that PAA-UCNP accumulated primarily in the liver and the spleen, and most of the PAA-UCNP could be slowly excreted from the mouse body over 3 months. No overt toxicity of PAA-UCNP in mice after long time exposure (up to 115 days) was detected based on body weight measurement and histological/hematological/biochemical analysis [49].

Considering that larger nanoparticle may behave differently *in vivo*, PAA coated UCNP with a larger diameter of 30 nm has also been studied in another report [110]. A similar biodistribution pattern was observed with virtually no noticeable toxic side effect, although the excretion rate was slower (< 50% of injected PAA-UCNP was cleared from mice body in 90 days). In both of the abovementioned reports [49, 110], evidence of eliminated PAA-UCNP in feces was not provided, which could have served as concrete evidence of hepatobiliary excretion. One drawback of such PAA-UCNP is the relatively short blood-circulation lifetime (< 10 min), which limited its potential for passive tumor targeting based on the enhanced permeability and retention (EPR) effect [111]. The use of erythrocyte membrane camouflaged UCNP may provide a potential solution for increasing the circulation lifetime.

More future investigation on the influence of particles size, shape, surface charge and coating on the biodistribution, clearance, and long term toxicity of UCNP should be carried out to evaluate the biocompatibility of this promising class of imaging probes. These abovementioned two reports paved the way for the future *in vivo* applications of UCNPs as multifunctional nanomedicine [49, 110]. Considering the extremely slow and variable hepatic clearance of PAA-UCNP, development of f-UCNP-based probes that could be eliminated by renal filtration may greatly speed up its clinical translation. Recent advances in the development of ultra-small QDs that can undergo renal clearance, successful synthesis of sub-10 nm sized $NaLuF_4$-based UCNP, and the recently approved clinical trial of

"Cornell Dots" (silica spheres < 8 nm in diameter that enclose several dye molecules) may provide insights and possible solutions to achieve this goal [41, 65, 112, 113].

UCNP FOR PARTICLE/CELL TRACKING

Photo-blinking, in which a single nanoprobe repeatedly becomes non-emissive for a finite length of time, is an intrinsic property of QDs that makes continuous real-time imaging difficult [114, 115]. The non-bleaching and non-blinking properties of one single UCNP was first reported by Wu *et al.* [38]. Diluted hydrophobic oleic acid capped hexagonal phase $NaYF_4$:Er^{3+}/Yb^{3+} (~26.9 nm) nanocrystals were dispersed on a silicon nitride membrane and spectroscopically imaged in a sample-scanning confocal optical microscope under the excitation by a tightly focused 980 nm CW laser. Combined with the images collected from transmission mode-scanning electron microscope (TM-SEM), it was demonstrated that the upconverted luminescent spots in ***Fig. (9A)*** was originated from one single UCNP. No photo-bleaching or photo-damage was observed even after 1 h of continuous 980 nm laser illumination (~5×10^6 W/cm^2) on one single UCNP (***Fig. (9B)***). Through the use of wide-field fluorescence microscopy and atomic force microscopy (AFM), Hyeon and co-workers also demonstrated such non-bleaching and non-blinking capabilities of one single UCNP (***Fig. (9C&D)***) [40].

Such remarkable photostability together with low cytotoxicity of UCNPs enabled real-time visualization of intracellular movements of UCNPs, as demonstrated through the use of amphiphilic PEG-phospholipids coated UCNPs as the tracking particles in single living HeLa cells [42]. No obvious cell death caused by continuous 980 nm laser illumination was observed, a prerequisite for real-time and long term particle tracking of UCNPs. On the other hand, illuminating the same cells with visible light (e.g. 532 nm laser) caused significant cell death. With a home-made epi-fluorescence microscope setup, the dynamic process of UCNPs in a single living cell was successfully imaged. It was found that most particles or their aggregates displayed random spatial fluctuations with relatively low amplitudes, while some underwent abrupt directed movements that typically lasted for a few seconds (***Fig. (10A)***). Further analysis suggested possible active transportation of UCNs by intracellular motor proteins walking on the microtubules (***Fig. (10B&C)***). Apart from phagocytosis which was exploited in this study, larger quantities of f-UCNP could potentially be delivered into living cells (or the cell nucleus) using various techniques such as microinjection [116], peptide-induced transport [117], and/or electroporation [118]. Although no *in vivo* long term particle (or cell) tracking has been explored yet using f-UCNP, the ability to image UCNPs at the single cell level holds tremendous potential for investigating stem cell movement, differentiation, and fate *in vivo* in the future, which may facilitate clinical translation of stem cell therapies.

REMOTE NIR LIGHT RESPONSIVE DRUG DELIVERY STSTEM BASED ON UCNP

To date, limited success has been demonstrated in constructing cancer killing nanosystems based on UCNP [50, 119-122], and none possesses a "smart" drug delivery strategy by taking advantage of UCNP's UCL features. Although conventional light-triggered drug delivery systems could potentially enable repeated, reproducible, on-demand dosing to achieve reduced systemic toxicity, these approaches require high-energy UV or visible light as the trigger which has limited tissue penetration and can result in tissue damage. With NIR laser excitation (980 nm), UCNP can emit UV to NIR light that can potentially act as an antenna (or a nano-transducer) for triggering functions and avoid tissue damage.

Since certain chemical changes (e.g. isomerization and bond cleavage) can only be achieved with light in the UV or visible range, most of the reported UCNP-based NIR laser-triggered nanosystems have focused on the use of such light emitted from $NaYF_4:Er^{3+}/Yb^{3+}$ or $NaYF_4:Tm^{3+}/Yb^{3+}$ nanoparticles. For example, remote 980 nm laser can control photo-switching of dithienylethene (DTE, a commonly used photo-switch between two structurally and electronically different isomers), using $NaYF_4:Tm^{3+}/Yb^{3+}$ (UV region) for ring-closing and $NaYF_4:Tm^{3+}/Yb^{3+}$ (visible region) for ring-opening, respectively [123]. Since the photoswitch does not absorb NIR light directly, the efficiency of UCNP-based photo-triggering system is largely dependent on the intensity of the UV upconversion emissions from the Tm^{3+} doped UCNPs. By using 980 nm laser with high power density (up to 500 W/cm^2) to excite $NaYF_4:Tm^{3+}/Yb^{3+}@NaYF_4:Er^{3+}/Yb^{3+}@NaYF_4$ for strong UV emission (***Fig. (11A)***), a more advanced and reversible photo-switching of DTE from ring-opening to ring-closing was achieved by modulating the intensity of the 980 nm excitation light (***Fig. (11B)***) [124].

980 nm laser induced photo-cleavage is another option for triggering the release of the active agent without directly using high-energy UV or blue light. Remote-controlled photo-release of caged compounds has been demonstrated, using $NaYF_4:Tm^{3+}/Yb^{3+}@NaYF_4$ nanoparticles where the emission spectrum (290 nm, UV region) partially overlaps with the absorption spectrum of 3',5'-di(carboxymethoxy) benzoin acetate (282 nm) [125]. Similar "drug" release in response to 980 nm light has also been achieved with block copolymer (BCP) micelles-encapsulated UCNPs, with UCNPs as the internal UV light source [126]. After loading of $NaYF_4:Tm^{3+}/Yb^{3+}$ and Nile Red inside the micelles and subsequent exposure to 980 nm light, photons in the UV region (emitted by the UCNPs) were absorbed by o-nitrobenzyl groups on the micelle and activated the photo-cleavage reaction, leading to the dissociation of BCP micelles and release of Nile Red.

Another category of 980 nm laser triggered drug delivery is based on the combination of photosensitizer (PS), NIR-light, and oxygen for initiating a photochemical reaction to generate toxic singlet oxygen ($^1O_2$) for cancer cell killing, a process known as photodynamic therapy (PDT) [127]. Since the first report on UCNP/M540 (i.e. Merocyanine-540) based PDT [104], only a few combinations of UCNP/PS have been reported and the quest for a better combination to improve the PDT efficiency has never stopped [128-133]. The first prototype of targeted UCNP/PS-based PDT drug was constructed by encapsulating M540 into a silica matrix using traditional Stöber method [104]. The loading capacity of M540 was limited due to the electrostatic repulsion between negatively charged M540 and the tetraethyl orthosilicate (TEOS) precursor. In a follow-up study, a simple non-covalent adsorption technique *via* hydrophobic interaction between ZnPC (Zinc phthalocyanine) and PEI (Poly(ethylene)imine) capped UCNP was developed [128]. By physically absorbing the same PS into mesoporous silica coated UCNP, the problems of low ZnPC loading and instability could be solved and NIR laser triggered production of $^1O_2$ was demonstrated [129]. To improve the PS loading capacity, another group replaced PEI with poly(ethylene glycol)-block -poly(caprolactone) (PEG-*b*-PCL) and poly(ethylene glycol-*block*-($_{DL}$)lactic acid) block copolymers (PEG-*b*-PLA) using their own UCNP/TPP (i.e. tetraphenyl porphine) combination and Flash NanoPrecipitation technique [130, 131]. Although preliminary *in vitro* PDT effect has been demonstrated in the aforementioned reports, *in vivo* therapeutic efficacy was not demonstrated until recently through the use of UCNP/Ce6 (i.e. Chlorin e6) combination (***Fig. (12)***) [132]. Convincing evidence of improved 980 nm laser-induced PDT effect in 4T1 tumor bearing mice over traditional PDT (using red light excitation) was provided, indicating great potential of UCNP/PS based drug for treating internal tumors. We recently reported a new UCNP/PS-based PDT drug, using brighter Gd^{3+} doped UCNP and water soluble methylene blue (MB) [133]. Successful "trapping" of the positively charged MB within the negatively charged

silica resulted in a core@shell structure of UCNP@SiO_2(MB) with attractive properties such as zero-PS-prerelease, 980 nm laser on-demand $^1O_2$ release, and combined UCL and MRI properties all integrated in a sub-50 nm sized multifunctional nanosystem.

CONCLUSION AND FUTURE PERSPECTIVES

Translational research is a continuum that bridges basic science discoveries and their potential clinical applications. The ultimate goal of translational research is to move novel imaging/therapeutic strategies/agents into clinical patient management. Molecular imaging plays indispensable roles in translational medicine. As a recently emerged versatile nanoplatform, translational research of f-UCNP is still at its infancy, yet it has already exhibited tremendous potential in preclinical research for both diagnostic and therapeutic applications. It is believed that f-UCNP can be used in place of traditional organic dyes and QDs in virtually any system and will outperform them in a majority of cases. The 2nd decade of the 21 st century is expected to witness even greater success in exploring potential applications of f-UCNP, such as multimodal targeted imaging of various diseases/pathways/targets, sensitive detection of circulating tumor cells, stem cell labeling and *in vivo* tracking, non-invasive real time therapeutic effect monitoring, among others. With the already demonstrated use of f-UCNP as nano-sensors for sensing temperature in a single cell [134], surrounding oxygen concentration [135], intracellular mercury ions and glutathione [136, 137], and avidin [37, 138], it is expected that not only multifunctional but also “smart” nano-devices based on f-UCNP will emerge in the near future.

Many challenges remain to be conquered for future broad applications of nano-systems or nano-devices based on f-UCNP. Further development and optimization in UCNP synthesis, surface coating, and bioconjugation will be needed for prolonging the blood circulation lifetime and creating high quality, renal excretable, and molecularly targeted f-UCNP that can be non-invasively detected by multiple imaging techniques. Targeting ligand-conjugated f-UCNP, labeled with long-lived PET isotopes, will be a desirable candidate for cancer early diagnosis and future clinical translation, if the concerns regarding biocompatibility, pharmacokinetics, *in vivo* targeting efficiency, cost-effectiveness, acute/chronic toxicity and clearance can all be adequately addressed.

To date, no *in vivo* tumor cell targeting based on f-UCNP has been reported yet owing to the relatively large size of probe. Optimization of particle size, surface characteristics, as well as the targeting efficiency *in vivo* deserves more research effort in the future. Decreasing the hydrodynamic diameter down to sub-10 nm will not only provide more opportunities for tumor cell targeting, but also open the avenue for renal clearance to minimize long term toxicity. Considering that most of the UCNP imaging systems (based on UCL) are home-made by employing an additional 980 nm laser module, commercialization of *in vivo* imaging system which can be used for whole-body imaging of UCNP in small animals will be very helpful for speeding up the development, application, and clinical translation of f-UCNP. Core-shell structured Gd^{3+} doped UCNP has been intensively studied. If the MRI sensitivity of these UCNP can be significantly improved to be applicable for *in vivo* targeted MRI, labeling the f-UCNP with PET isotopes will provide perhaps the most useful multimodality agents (i.e. PET/MRI/UCL) that can offer extremely high sensitivity (PET), exquisite soft tissue contrast (MRI), surgical guidance (UCL), convenient histological validation (UCL), among others.

Cancer is a complex disease that involves an elaborate interplay of genetic mutations and epigenetic alterations that can affect the behavior and regulation of many genes. Individuals of the same cancer type and at the same stage do not necessarily carry the same cancer-triggering mutations. Stratification of patients on the molecular level using targeted

(multimodality) molecular imaging probes is a vital step for future personalized therapy. F-UCNP may present one of the best candidates for detecting molecular or physiological alterations which could signal the presence and/or metastasis of certain cancers, delivering drugs for cancer cell killing in a (remotely) controllable manner, as well as evaluating and adjusting the treatment protocol in real time. More effective collaborations among cellular/molecular biologists, chemists/radiochemists, engineers, material scientists, etc. are necessary to foster the continued discovery, development, and future translation of f-UCNP based imaging probes (or drugs).

Acknowledgments

We gratefully acknowledge financial supports from the National Natural Science Foundation of China Research (Grant No. 50823007, 50972154, 51132009, 51072212, 51102259, 21172043), the Science and Technology Commission of Shanghai (Grant No. 11nm0505000, 10430712800), the National Basic Research Program of China (973 Program, Grant No.2011CB707905).

REFERENCES

1. Nie S, Xing Y, Kim GJ, Simons JW. Nanotechnology applications in cancer. Ann Rev B E. 2007:257–88.
2. Ferrari M. Cancer nanotechnology: Opportunities and challenges. Nat Rev Cancer. 2005; 5:161–71. [PubMed: 15738981]
3. Brigger I, Dubernet C, Couvreur P. Nanoparticles in cancer therapy and diagnosis. Adv Drug Deliv Rev. 2002; 54:631–51. [PubMed: 12204596]
4. Massoud TF, Gambhir SS. Molecular imaging in living subjects: seeing fundamental biological processes in a new light. Genes Dev. 2003; 17:545–80. [PubMed: 12629038]
5. Alauddin MM. Positron emission tomography (PET) imaging with ^{18}F-based radiotracers. Am J Nucl Med Mol Imaging. 2012; 2:55–76. [PubMed: 23133802]
6. Grassi I, Nanni C, Allegri V, et al. The clinical use of PET with ^{11}C-acetate. Am J Nucl Med Mol Imaging. 2012; 2:33–47. [PubMed: 23133801]
7. Eary JF, Hawkins DS, Rodler ET, Conrad EUI. ^{18}F-FDG PET in sarcoma treatment response imaging. Am J Nucl Med Mol Imaging. 2011; 1:47–53. [PubMed: 23133794]
8. Bhargava P, He G, Samarghandi A, Delpassand ES. Pictorial review of SPECT/CT imaging applications in clinical nuclear medicine. Am J Nucl Med Mol Imaging. 2012; 2:221–31. [PubMed: 23133813]
9. Aparici CM, Carlson D, Nguyen N, Hawkins RA, Seo Y. Combined SPECT and Multidetector CT for Prostate Cancer Evaluations. Am J Nucl Med Mol Imaging. 2012; 2:48–54. [PubMed: 22267999]
10. Chin PTK, Beekman CAC, Buckle T, Josephson L, van Leeuwen FWB. Multispectral visualization of surgical safety-margins using fluorescent marker seeds. Am J Nucl Med Mol Imaging. 2012; 2:151–62. [PubMed: 23133810]
11. Huang X, Lee S, Chen X. Design of “smart” probes for optical imaging of apoptosis. Am J Nucl Med Mol Imaging. 2011; 1:3–17. [PubMed: 22514789]
12. Cai WB, Rao JH, Gambhir SS, Chen XY. How molecular imaging is speeding up antiangiogenic drug development. Mol Cancer Ther. 2006; 5:2624–33. [PubMed: 17121909]
13. Tandon P, Nordstrom RJ. Next-generation imaging development for nanoparticle biodistribution measurements. Wiley Interdiscip Rev Nanomed Nanobiotechnol. 2011; 3:5–10. [PubMed: 20842710]
14. Weissleder R. Molecular Imaging in Cancer. Science. 2006; 312:1168–71. [PubMed: 16728630]
15. Rudin M, Weissleder R. Molecular imaging in drug discovery and development. Nat Rev Drug Discov. 2003; 2:123–31. [PubMed: 12563303]
16. Cai WB, Chen XY. Nanoplatforms for targeted molecular imaging in living subjects. Small. 2007; 3:1840–54. [PubMed: 17943716]

17. Abeylath SC, Ganta S, Iyer AK, Amiji M. Combinatorial-Designed Multifunctional Polymeric Nanosystems for Tumor-Targeted Therapeutic Delivery. Acc Chem Res. 2011; 44:1009–17. [PubMed: 21761902]
18. Al-Jamal WT, Kostarelos K. Liposomes: From a Clinically Established Drug Delivery System to a Nanoparticle Platform for Theranostic Nanomedicine. Acc Chem Res. 2011; 44:1094–104. [PubMed: 21812415]
19. Ambrogio MW, Thomas CR, Zhao Y-L, Zink JI, Stoddart JF. Mechanized Silica Nanoparticles: A New Frontier in Theranostic Nanomedicine. Acc Chem Res. 2011; 44:903–13. [PubMed: 21675720]
20. Bardhan R, Lal S, Joshi A, Halas NJ. Theranostic Nanoshells: From Probe Design to Imaging and Treatment of Cancer. Acc Chem Res. 2011; 44:936–46. [PubMed: 21612199]
21. Barreto JA, O'Malley W, Kubeil M, et al. Nanomaterials: Applications in Cancer Imaging and Therapy. Adv Mater. 2011; 23:H18–H40. [PubMed: 21433100]
22. Cabral H, Nishiyama N, Kataoka K. Supramolecular Nanodevices: From Design Validation to Theranostic Nanomedicine. Acc Chem Res. 2011; 44:999–1008. [PubMed: 21755933]
23. Cheng Y, Zhao L, Li Y, Xu T. Design of biocompatible dendrimers for cancer diagnosis and therapy: current status and future perspectives. Chem Soc Rev. 2011; 40:2673–703. [PubMed: 21286593]
24. Della Rocca J, Liu D, Lin W. Nanoscale Metal–Organic Frameworks for Biomedical Imaging and Drug Delivery. Acc Chem Res. 2011; 44:957–68. [PubMed: 21648429]
25. Dreaden EC, Mackey MA, Huang X, Kang B, El-Sayed MA. Beating cancer in multiple ways using nanogold. Chem Soc Rev. 2011; 40:3391–404. [PubMed: 21629885]
26. Ho D, Sun X, Sun S. Monodisperse Magnetic Nanoparticles for Theranostic Applications. Acc Chem Res. 2011; 44:875–82. [PubMed: 21661754]
27. Lee JE, Lee N, Kim T, Kim J, Hyeon T. Multifunctional Mesoporous Silica Nanocomposite Nanoparticles for Theranostic Applications. Acc Chem Res. 2011; 44:893–902. [PubMed: 21848274]
28. Xia Y, Li W, Cobley CM, et al. Gold Nanocages: From Synthesis to Theranostic Applications. Acc Chem Res. 2011; 44:914–24. [PubMed: 21528889]
29. Yoo D, Lee J-H, Shin T-H, Cheon J. Theranostic Magnetic Nanoparticles. Acc Chem Res. 2011; 44:863–74. [PubMed: 21823593]
30. Sun M, Hoffman D, Sundaresan G, et al. Synthesis and characterization of intrinsically radio-labeled quantum dots for bimodal detection. Am J Nucl Med Mol Imaging. 2012; 2:122–35. [PubMed: 23133807]
31. Cai W, Hong H. In a “nutshell”: intrinsically radio-labeled quantum dots. Am J Nucl Med Mol Imaging. 2012; 2:136–40. [PubMed: 23133808]
32. Yigit MV, Medarova Z. In vivo and ex vivo applications of gold nanoparticles for biomedical SERS imaging. Am J Nucl Med Mol Imaging. 2012; 2:232–41. [PubMed: 23133814]
33. Zhou J, Liu Z, Li F. Upconversion nanophosphors for small-animal imaging. Chem Soc Rev. 2012; 41:1323–49. [PubMed: 22008740]
34. Auzel F. Upconversion and Anti-Stokes Processes with f and d Ions in Solids. Chem Rev. 2003; 104:139–74. [PubMed: 14719973]
35. Haase M, Schäfer H. Upconverting Nanoparticles. Angew Chem Int Ed. 2011; 50:5808–29.
36. Wang J, Wang F, Wang C, Liu Z, Liu XG. Single-Band Upconversion Emission in Lanthanide-Doped KMnF(3) Nanocrystals. Angew Chem Int Ed. 2011; 50:10369–72.
37. Ju Q, Tu D, Liu Y, et al. Amine-Functionalized Lanthanide-Doped KGdF4 Nanocrystals as Potential Optical/Magnetic Multimodal Bioprobes. J Am Chem Soc. 2011; 134:1323–30. [PubMed: 22145918]
38. Wu SW, Han G, Milliron DJ, et al. Non-blinking and photostable upconverted luminescence from single lanthanide-doped nanocrystals. Proc Natl Acad Sci USA. 2009; 106:10917–21. [PubMed: 19541601]
39. Cheng LA, Yang K, Zhang SA, et al. Highly-Sensitive Multiplexed in vivo Imaging Using PEGylated Upconversion Nanoparticles. Nano Res. 2010; 3:722–32.

40. Park YI, Kim JH, Lee KT, et al. Nonblinking and Nonbleaching Upconverting Nanoparticles as an Optical Imaging Nanoprobe and T1 Magnetic Resonance Imaging Contrast Agent. Adv Mater. 2009; 21:4467–71.
41. Liu Q, Sun Y, Yang T, et al. Sub-10 nm Hexagonal Lanthanide-Doped NaLuF4 Upconversion Nanocrystals for Sensitive Bioimaging in Vivo. J Am Chem Soc. 2011; 133:17122–5. [PubMed: 21957992]
42. Nam SH, Bae YM, Park YI, et al. Long-Term Real-Time Tracking of Lanthanide Ion Doped Upconverting Nanoparticles in Living Cells. Angew Chem Int Ed. 2011; 50:6093–7.
43. Xiong L, Chen Z, Tian Q, et al. High Contrast Upconversion Luminescence Targeted Imaging in Vivo Using Peptide-Labeled Nanophosphors. Anal Chem. 2009; 81:8687–94. [PubMed: 19817386]
44. Kobayashi H, Kosaka N, Ogawa M, et al. In vivo multiple color lymphatic imaging using upconverting nanocrystals. J Mater Chem. 2009; 19:6481–4.
45. Kumar R, Nyk M, Ohulchanskyy TY, Flask CA, Prasad PN. Combined Optical and MR Bioimaging Using Rare Earth Ion Doped NaYF4 Nanocrystals. Adv Funct Mater. 2009; 19:853–9.
46. Chen F, Bu W, Zhang S, et al. Positive and Negative Lattice Shielding Effects Co-existing in Gd (III) Ion Doped Bifunctional Upconversion Nanoprobes. Adv Funct Mater. 2011; 21:4285–94.
47. Gorris HH, Ali R, Saleh SM, Wolfbeis OS. Tuning the Dual Emission of Photon-Upconverting Nanoparticles for Ratiometric Multiplexed Encoding. Adv Mater. 2011; 23:1652–5. [PubMed: 21472793]
48. Zhang F, Shi Q, Zhang Y, et al. Fluorescence Upconversion Microbarcodes for Multiplexed Biological Detection: Nucleic Acid Encoding. Adv Mater. 2011; 23:3775–9.
49. Xiong L, Yang T, Yang Y, Xu C, Li F. Long-term in vivo biodistribution imaging and toxicity of polyacrylic acid-coated upconversion nanophosphors. Biomaterials. 2010; 31:7078–85. [PubMed: 20619791]
50. Cheng L, Yang K, Li Y, et al. Facile Preparation of Multifunctional Upconversion Nanoprobes for Multimodal Imaging and Dual-Targeted Photothermal Therapy. Angew Chem Int Ed. 2011; 50:7385–90.
51. Liu Y, Ai K, Liu J, et al. A High-Performance Ytterbium-Based Nanoparticulate Contrast Agent for In Vivo X-Ray Computed Tomography Imaging. Angew Chem Int Ed. 2012; 51:1437–42.
52. Chatterjee DK, Rufaihah AJ, Zhang Y. Upconversion fluorescence imaging of cells and small animals using lanthanide doped nanocrystals. Biomaterials. 2008; 29:937–43. [PubMed: 18061257]
53. Wang F, Banerjee D, Liu YS, Chen XY, Liu XG. Upconversion nanoparticles in biological labeling, imaging, and therapy. Analyst. 2010; 135:1839–54. [PubMed: 20485777]
54. Mai HX, Zhang YW, Si R, et al. High-quality sodium rare-earth fluoride nanocrystals: Controlled synthesis and optical properties. J Am Chem Soc. 2006; 128:6426–36. [PubMed: 16683808]
55. Qian HS, Zhang Y. Synthesis of Hexagonal-Phase Core-Shell NaYF4 Nanocrystals with Tunable Upconversion Fluorescence. Langmuir. 2008; 24:12123–5. [PubMed: 18839973]
56. Boyer JC, Cuccia LA, Capobianco JA. Synthesis of colloidal upconverting NaYF4 : Er3+/Yb3+ and Tm3+/Yb3+ monodisperse nanocrystals. Nano Lett. 2007; 7:847–52. [PubMed: 17302461]
57. Li ZQ, Zhang Y. An efficient and user-friendly method for the synthesis of hexagonal-phase NaYF4 : Yb, Er/Tm nanocrystals with controllable shape and upconversion fluorescence. Nanotechnology. 2008; 19:5.
58. Wang F, Han Y, Lim CS, et al. Simultaneous phase and size control of upconversion nanocrystals through lanthanide doping. Nature. 2010; 463:1061–5. [PubMed: 20182508]
59. Wang X, Zhuang J, Peng Q, Li YD. A general strategy for nanocrystal synthesis. Nature. 2005; 437:121–4. [PubMed: 16136139]
60. Wang F, Wang J, Liu X. Direct Evidence of a Surface Quenching Effect on Size-Dependent Luminescence of Upconversion Nanoparticles. Angew Chem Int Ed. 2010; 49:7456–60.
61. Wang F, Deng R, Wang J, et al. Tuning upconversion through energy migration in core–shell nanoparticles. Nat Mater. 2011; 10:968–73. [PubMed: 22019945]

62. Chen G, Ohulchanskyy TY, Kumar R, Ågren H, Prasad PN. Ultrasmall Monodisperse NaYF4:Yb3+/Tm3+ Nanocrystals with Enhanced Near-Infrared to Near-Infrared Upconversion Photoluminescence. ACS Nano. 2010; 4:3163–8. [PubMed: 20509664]
63. Johnson NJJ, Oakden W, Stanisz GJ, Scott Prosser R, van Veggel FCJM. Size-Tunable, Ultrasmall NaGdF4 Nanoparticles: Insights into Their T1 MRI Contrast Enhancement. Chem Mater. 2011; 23:3714–22.
64. Boyer J-C, van Veggel FCJM. Absolute quantum yield measurements of colloidal NaYF4: Er3+, Yb3+ upconverting nanoparticles. Nanoscale. 2010; 2:1417–9. [PubMed: 20820726]
65. Soo Choi H, Liu W, Misra P, et al. Renal clearance of quantum dots. Nat Biotech. 2007; 25:1165–70.
66. Guo H, Li ZQ, Qian HS, Hu Y, Muhammad IN. Seed-mediated synthesis of NaYF(4):Yb, Er/NaGdF(4) nanocrystals with improved upconversion fluorescence and MR relaxivity. Nanotechnology. 2010; 21:125602–8. [PubMed: 20182011]
67. Abel KA, Boyer J-C, Veggel FCJMv. Hard Proof of the NaYF4/NaGdF4 Nanocrystal Core/Shell Structure. J Am Chem Soc. 2009; 131:14644–5. [PubMed: 19824725]
68. Abel KA, Boyer J-C, Andrei CM, van Veggel FCJM. Analysis of the Shell Thickness Distribution on NaYF4/NaGdF4 Core/Shell Nanocrystals by EELS and EDS. J Phys Chem Lett. 2011; 2:185–9.
69. Zhang Y, Hong H, Engle JW, et al. Positron emission tomography and near-infrared fluorescence imaging of vascular endothelial growth factor with dual-labeled bevacizumab. Am J Nucl Med Mol Imaging. 2012; 2:1–13. [PubMed: 22229128]
70. Thorek DLJ, Robertson R, Bacchus WA, et al. Cerenkov imaging - a new modality for molecular imaging. Am J Nucl Med Mol Imaging. 2012; 2:163–73. [PubMed: 23133811]
71. Cai W, Zhang Y, Kamp TJ. Imaging of induced pluripotent stem cells: from cellular reprogramming to transplantation. Am J Nucl Med Mol Imaging. 2011; 1:18–28. [PubMed: 21841970]
72. Zhang Y, Cai W. Molecular imaging of insulin-like growth factor 1 receptor in cancer. Am J Nucl Med Mol Imaging. 2012; 2:248–59. [PubMed: 23066521]
73. Nyk M, Kumar R, Ohulchanskyy TY, Bergey EJ, Prasad PN. High Contrast in Vitro and in Vivo Photoluminescence Bioimaging Using Near Infrared to Near Infrared Up-Conversion in TM3+ and Yb3+ Doped Fluoride Nanophosphors. Nano Lett. 2008; 8:3834–8. [PubMed: 18928324]
74. Zhou J, Sun Y, Du XX, et al. Dual-modality in vivo imaging using rare-earth nanocrystals with near-infrared to near-infrared (NIR-to-NIR) upconversion luminescence and magnetic resonance properties. Biomaterials. 2010; 31:3287–95. [PubMed: 20132982]
75. Xing H, Bu W, Zhang S, et al. Multifunctional nanoprobes for upconversion fluorescence, MR and CT trimodal imaging. Biomaterials. 2012; 33:1079–89. [PubMed: 22061493]
76. Chen F, Zhang S, Bu W, et al. A “Neck-Formation” Strategy for an Antiquenching Magnetic/Upconversion Fluorescent Bimodal Cancer Probe. Chem Eur J. 2010; 16:11254–60. [PubMed: 20715197]
77. Xia A, Gao Y, Zhou J, et al. Core–shell NaYF4:Yb3+,Tm3+@FexOy nanocrystals for dual-modality T2-enhanced magnetic resonance and NIR-to-NIR upconversion luminescent imaging of small-animal lymphatic node. Biomaterials. 2011; 32:7200–8. [PubMed: 21742376]
78. Hou Z, Li C, Ma P, et al. Electrospinning Preparation and Drug-Delivery Properties of an Up-conversion Luminescent Porous NaYF4:Yb3+, Er3+@Silica Fiber Nanocomposite. Adv Funct Mater. 2011; 21:2356–65.
79. Tian G, Gu Z, Zhou L, et al. Mn2+ Dopant-Controlled Synthesis of NaYF4:Yb/Er Upconversion Nanoparticles for in vivo Imaging and Drug Delivery. Adv Mater. 2012; 24:1226–31. [PubMed: 22282270]
80. Shen J, Sun L-D, Zhu J-D, et al. Biocompatible Bright YVO4:Eu Nanoparticles as Versatile Optical Bioprobes. Adv Funct Mater. 2010; 20:3708–14.
81. Wang J, Wang F, Wang C, Liu Z, Liu X. Single-Band Upconversion Emission in Lanthanide-Doped KMnF(3) Nanocrystals. Angew Chem Int Ed. 2011; 50:10369–72.

82. He M, Huang P, Zhang C, et al. Dual Phase-Controlled Synthesis of Uniform Lanthanide-Doped NaGdF4 Upconversion Nanocrystals Via an OA/Ionic Liquid Two-Phase System for In Vivo Dual-Modality Imaging. Adv Funct Mater. 2011; 21:4470–7.
83. Zhu X, Zhou J, Chen M, et al. Core–shell Fe3O4@NaLuF4:Yb,Er/Tm nanostructure for MRI, CT and upconversion luminescence tri-modality imaging. Biomaterials. 2012; 33:4618–27. [PubMed: 22444645]
84. Xing H, Bu W, Ren Q, et al. A NaYbF4: Tm3+ nanoprobe for CT and NIR-to-NIR fluorescent bimodal imaging. Biomaterials. 2012 Published online.
85. Haller C, Hizoh I. The cytotoxicity of iodinated radiocontrast agents on renal cells in vitro. Invest Radiol. 2004; 39:149–54. [PubMed: 15076007]
86. Hizoh I, Haller C. Radiocontrast-induced renal tubular cell apoptosis - Hypertonic versus oxidative stress. Invest Radiol. 2002; 37:428–34. [PubMed: 12138358]
87. Liu Q, Chen M, Sun Y, et al. Multifunctional rare-earth self-assembled nanosystem for tri-modal upconversion luminescence/fluorescence/positron emission tomography imaging. Biomaterials. 2011; 32:8243–53. [PubMed: 21820170]
88. Liu Q, Sun Y, Li CG, et al. (18)F-Labeled Magnetic-Upconversion Nanophosphors via Rare-Earth Cation-Assisted Ligand Assembly. ACS Nano. 2011; 5:3146–57. [PubMed: 21384900]
89. Sun Y, Yu M, Liang S, et al. Fluorine-18 labeled rare-earth nanoparticles for positron emission tomography (PET) imaging of sentinel lymph node. Biomaterials. 2011; 32:2999–3007. [PubMed: 21295345]
90. Zhou J, Yu M, Sun Y, et al. Fluorine-18-labeled Gd(3+)/Yb(3+)/Er(3+) co-doped NaYF(4) nanophosphors for multimodality PET/MRI/UCL imaging. Biomaterials. 2011; 32:1148–56. [PubMed: 20965563]
91. Buckle T, van den Berg NS, Kuil J, et al. Non-invasive longitudinal imaging of tumor progression using an ^{111}indium labeled CXCR4 peptide antagonist. Am J Nucl Med Mol Imaging. 2012; 2:99–109. [PubMed: 23133805]
92. Cai W, Hong H. Peptoid and positron emission tomography: an appealing combination. Am J Nucl Med Mol Imaging. 2011; 1:76–9. [PubMed: 22022661]
93. Hong H, Zhang Y, Engle JW, et al. In vivo targeting and positron emission tomography imaging of tumor vasculature with (66)Ga-labeled nano-graphene. Biomaterials. 2012; 33:4147–56. [PubMed: 22386918]
94. Hong H, Severin GW, Yang Y, et al. Positron emission tomography imaging of CD105 expression with 89Zr-Df-TRC105. Eur J Nucl Med Mol Imaging. 2012; 39:138–48. [PubMed: 21909753]
95. Hall H, Velikyan I, Blom E, et al. In vitro autoradiography of carcinoembryonic antigen in tissue from patients with colorectal cancer using multifunctional antibody TF2 and 67/68Ga-labeled haptens by pretargeting. Am J Nucl Med Mol Imaging. 2012; 2:141–50. [PubMed: 23133809]
96. Hao G, Hajibeigi A, De León-Rodríguez LM, Öz OK, Sun X. Peptoid-based PET imaging of vascular endothelial growth factor receptor (VEGFR) expression. Am J Nucl Med Mol Imaging. 2011; 1:65–75. [PubMed: 23133797]
97. Zhao R, Wang J, Deng J, Yang W, Wang J. Efficacy of ^{99m}Tc-EDDA/HYNIC-TOCSPECT/CT scintigraphy in Graves' ophthalmopathy. Am J Nucl Med Mol Imaging. 2012; 2:242–7. [PubMed: 23133815]
98. Cao TY, Yang Y, Gao YA, et al. High-quality water-soluble and surface-functionalized upconversion nanocrystals as luminescent probes for bioimaging. Biomaterials. 2011; 32:2959–68. [PubMed: 21262531]
99. Wang C, Cheng LA, Liu ZA. Drug delivery with upconversion nanoparticles for multi-functional targeted cancer cell imaging and therapy. Biomaterials. 2011; 32:1110–20. [PubMed: 20965564]
100. Hu H, Xiong L, Zhou J, et al. Multimodal-Luminescence Core–Shell Nanocomposites for Targeted Imaging of Tumor Cells. Chem Eur J. 2009; 15:3577–84. [PubMed: 19219877]
101. Zhan QQ, Qian J, Liang HJ, et al. Using 915 nm Laser Excited Tm(3+)/Er(3+)/Ho(3+)-Doped NaYbF4 Upconversion Nanoparticles for in Vitro and Deeper in Vivo Bioimaging without Overheating Irradiation. ACS Nano. 2011; 5:3744–57. [PubMed: 21513307]

102. Wang M, Mi CC, Wang WX, et al. Immunolabeling and NIR-Excited Fluorescent Imaging of HeLa Cells by Using NaYF(4):Yb,Er Upconversion Nanoparticles. ACS Nano. 2009; 3:1580–6. [PubMed: 19476317]
103. Jiang S, Zhang Y, Lim KM, Sim EKW, Ye L. NIR-to-visible upconversion nanoparticles for fluorescent labeling and targeted delivery of siRNA. Nanotechnology. 2009; 20:155101–9. [PubMed: 19420539]
104. Zhang P, Steelant W, Kumar M, Scholfield M. Versatile Photosensitizers for Photodynamic Therapy at Infrared Excitation. J Am Chem Soc. 2007; 129:4526–7. [PubMed: 17385866]
105. Xiong L-Q, Chen Z-G, Yu M-X, et al. Synthesis, characterization, and in vivo targeted imaging of amine-functionalized rare-earth up-converting nanophosphors. Biomaterials. 2009; 30:5592–600. [PubMed: 19564039]
106. Yu X-F, Sun Z, Li M, et al. Neurotoxin-conjugated upconversion nanoprobes for direct visualization of tumors under near-infrared irradiation. Biomaterials. 2010; 31:8724–31. [PubMed: 20728213]
107. Cai WB, Chen XY. Multimodality molecular imaging of tumor angiogenesis. J Nucl Med. 2008; 49:113S–28S. [PubMed: 18523069]
108. Cai WB, Shin DW, Chen K, et al. Peptide-labeled near-infrared quantum dots for imaging tumor vasculature in living subjects. Nano Lett. 2006; 6:669–76. [PubMed: 16608262]
109. Dong N-N, Pedroni M, Piccinelli F, et al. NIR-to-NIR Two-Photon Excited CaF2:Tm3+,Yb3+ Nanoparticles: Multifunctional Nanoprobes for Highly Penetrating Fluorescence Bio-Imaging. ACS Nano. 2011; 5:8665–71. [PubMed: 21957870]
110. Cheng L, Yang K, Shao MW, Lu XH, Liu Z. In vivo pharmacokinetics, long-term biodistribution and toxicology study of functionalized upconversion nanoparticles in mice. Nanomedicine. 2011; 6:1327–40. [PubMed: 21834646]
111. Fang J, Nakamura H, Maeda H. The EPR effect: Unique features of tumor blood vessels for drug delivery, factors involved, and limitations and augmentation of the effect. Adv Drug Deliv Rev. 2011; 63:136–51. [PubMed: 20441782]
112. Choi HS, Liu WH, Liu FB, et al. Design considerations for tumour-targeted nanoparticles. Nat Nanotechnol. 2010; 5:42–7. [PubMed: 19893516]
113. Benezra M, Penate-Medina O, Zanzonico PB, et al. Multimodal silica nanoparticles are effective cancer-targeted probes in a model of human melanoma. J Clin Invest. 2011; 121:2768–80. [PubMed: 21670497]
114. Pelton M, Smith G, Scherer NF, Marcus RA. Evidence for a diffusion-controlled mechanism for fluorescence blinking of colloidal quantum dots. Proc Natl Acad Sci USA. 2007; 104:14249–54. [PubMed: 17720807]
115. Yao J, Larson DR, Vishwasrao HD, Zipfel WR, Webb WW. Blinking and nonradiant dark fraction of water-soluble quantum dots in aqueous solution. Proc Natl Acad Sci USA. 2005; 102:14284–9. [PubMed: 16169907]
116. Dubertret B, Skourides P, Norris DJ, et al. In vivo imaging of quantum dots encapsulated in phospholipid micelles. Science. 2002; 298:1759–62. [PubMed: 12459582]
117. Mattheakis LC, Dias JM, Choi YJ, et al. Optical coding of mammalian cells using semiconductor quantum dots. Anal Biochem. 2004; 327:200–8. [PubMed: 15051536]
118. Ramachandran S, Merrill NE, Blick RH, van der Weide DW. Colloidal quantum dots initiating current bursts in lipid bilayers. Biosens Bioelectron. 2005; 20:2173–6. [PubMed: 15741094]
119. Zhang F, Braun GB, Pallaoro A, et al. Mesoporous Multifunctional Upconversion Luminescent and Magnetic “Nanorattle” Materials for Targeted Chemotherapy. Nano Lett. 2011; 12:61–7. [PubMed: 22133237]
120. Liu J, Bu W, Zhang S, et al. Controlled Synthesis of Uniform and Monodisperse Upconversion Core/Mesoporous Silica Shell Nanocomposites for Bimodal Imaging. Chem Eur J. 2012; 18:2335–41. [PubMed: 22252972]
121. Gai S, Yang P, Li C, et al. Synthesis of Magnetic, Up-Conversion Luminescent, and Mesoporous Core–Shell-Structured Nanocomposites as Drug Carriers. Adv Funct Mater. 2010; 20:1166–72.

122. Dai Y, Ma Pa, Cheng Z, et al. Up-Conversion Cell Imaging and pH-Induced Thermally Controlled Drug Release from NaYF4:Yb3+/Er3+@Hydrogel Core–Shell Hybrid Microspheres. ACS Nano. 2012; 6:3327–38. [PubMed: 22435911]
123. Carling C-J, Boyer J-C, Branda NR. Remote-Control Photoswitching Using NIR Light. J Am Chem Soc. 2009; 131:10838–39. [PubMed: 19722663]
124. Boyer J-C, Carling C-J, Gates BD, Branda NR. Two-Way Photoswitching Using One Type of Near-Infrared Light, Upconverting Nanoparticles, and Changing Only the Light Intensity. J Am Chem Soc. 2010; 132:15766–72. [PubMed: 20949969]
125. Carling C-J, Nourmohammadian F, Boyer J-C, Branda NR. Remote-Control Photorelease of Caged Compounds Using Near-Infrared Light and Upconverting Nanoparticles. Angew Chem Int Ed. 2010; 49:3782–5.
126. Wu W, Yao L, Yang T, et al. NIR-Light-Induced Deformation of Cross-Linked Liquid-Crystal Polymers Using Upconversion Nanophosphors. J Am Chem Soc. 2011; 133:15810–3. [PubMed: 21913658]
127. Agostinis P, Berg K, Cengel KA, et al. Photodynamic therapy of cancer: An update. CA Cancer J Clin. 2011; 61:250–81. [PubMed: 21617154]
128. Chatterjee DK, Yong Z. Upconverting nanoparticles as nanotransducers for photodynamic therapy in cancer cells. Nanomedicine. 2008; 3:73–82. [PubMed: 18393642]
129. Qian HS, Guo HC, Ho PC-L, Mahendran R, Zhang Y. Mesoporous-Silica-Coated Up-Conversion Fluorescent Nanoparticles for Photodynamic Therapy. Small. 2009; 5:2285–90. [PubMed: 19598161]
130. Ungun B, Prud'homme RK, Budijono SJ, et al. Nanofabricated upconversion nanoparticles for photodynamic therapy. Opt Express. 2009; 17:80–6. [PubMed: 19129875]
131. Shan J, Budijono SJ, Hu G, et al. Pegylated Composite Nanoparticles Containing Upconverting Phosphors and meso-Tetraphenyl porphine (TPP) for Photodynamic Therapy. Adv Funct Mater. 2011; 21:2488–95.
132. Wang C, Tao H, Cheng L, Liu Z. Near-infrared light induced in vivo photodynamic therapy of cancer based on upconversion nanoparticles. Biomaterials. 2011; 32:6145–54. [PubMed: 21616529]
133. Chen F, Zhang S, Bu W, et al. A Uniform Sub-50 nm-Sized Magnetic/Upconversion Fluorescent Bimodal Imaging Agent Capable of Generating Singlet Oxygen by Using a 980 nm Laser. Chem Eur J. 2012 DOI: 10.1002/chem.201103611.
134. Vetrone F, Naccache R, Zamarrón A, et al. Temperature Sensing Using Fluorescent Nanothermometers. ACS Nano. 2010; 4:3254–8. [PubMed: 20441184]
135. Achatz DE, Meier RJ, Fischer LH, Wolfbeis OS. Luminescent Sensing of Oxygen Using a Quenchable Probe and Upconverting Nanoparticles. Angew Chem Int Ed. 2011; 50:260–3.
136. Deng R, Xie X, Vendrell M, Chang Y-T, Liu X. Intracellular Glutathione Detection Using MnO2-Nanosheet-Modified Upconversion Nanoparticles. J Am Chem Soc. 2011; 133:20168–71. [PubMed: 22107163]
137. Liu Q, Peng J, Sun L, Li F. High-Efficiency Upconversion Luminescent Sensing and Bioimaging of Hg(II) by Chromophoric Ruthenium Complex-Assembled Nanophosphors. ACS Nano. 2011; 5:8040–8. [PubMed: 21899309]
138. Tu D, Liu L, Ju Q, et al. Time-Resolved FRET Biosensor Based on Amine-Functionalized Lanthanide-Doped NaYF4 Nanocrystals. Angew Chem Int Ed. 2011; 50:6306–10.

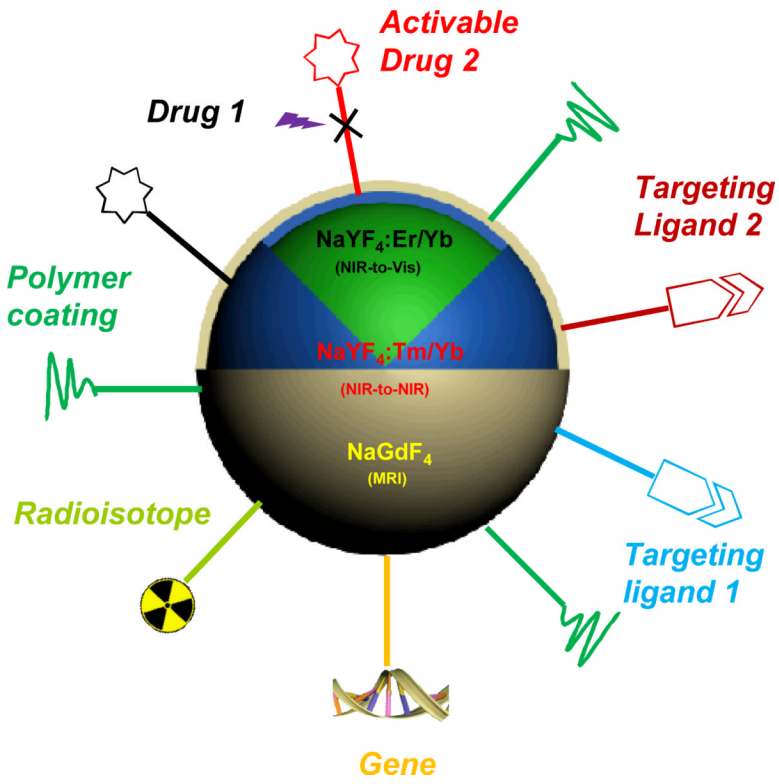

Scheme 1.

A schematic illustration of functionalized upconversion nanoparticle (f-UCNP). A core@multi-shell UCNP is designed as the starting point for integrated multicolor UCL imaging and MRI. The inner-most core is $NaYF_4:Er^{3+}/Yb^{3+}$ (for NIR-to-Vis optical imaging); the first shell is $NaYF_4:Tm^{3+}/Yb^{3+}$ (for NIR-to-NIR optical imaging); the second shell is $NaGdF_4$ (for MRI). With the presence of designed active sites on the surface of UCNP, polymer coating (such as a PEG layer for stealth capability), radioisotopes (such as ^{64}Cu for highly sensitive PET imaging), (light cleavable) anticancer drugs/genes for cancer cell killing, single or combined targeting ligands (for multiple receptor targeting) can be conjugated to yield a multifunctional nanoplatform for molecular imaging and therapy applications.

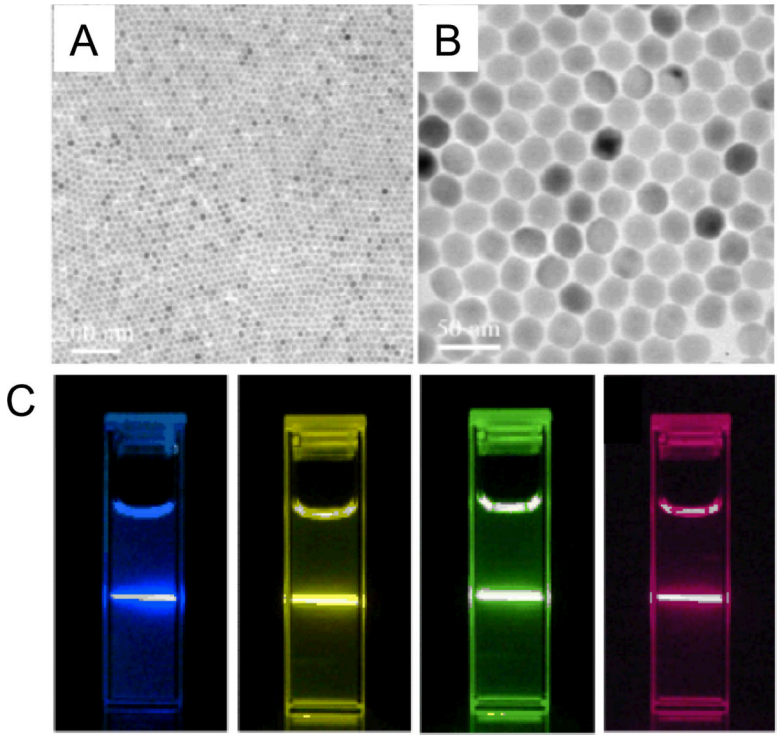

Fig. (1).

Represent TEM images of $NaYF_4$:Yb^{3+}/Er^{3+} nanospheres at low (A) and high (B) magnifications. (C) Photographs of the nanospheres in hexane under the excitation of a 980 nm laser. From left to right: total upconversion fluorescence of $NaYF_4$:Yb^{3+}/Tm^{3+} (25/0.3 mol%) nanospheres, total upconversion fluorescence of $NaYF_4$:Yb^{3+}/Er^{3+} (18/2 mol%) nanospheres, and fluorescence of $NaYF_4$:Yb^{3+}/Er^{3+} (18/2 mol%) nanospheres passing through red and green filters. Reprinted with permission from [57].

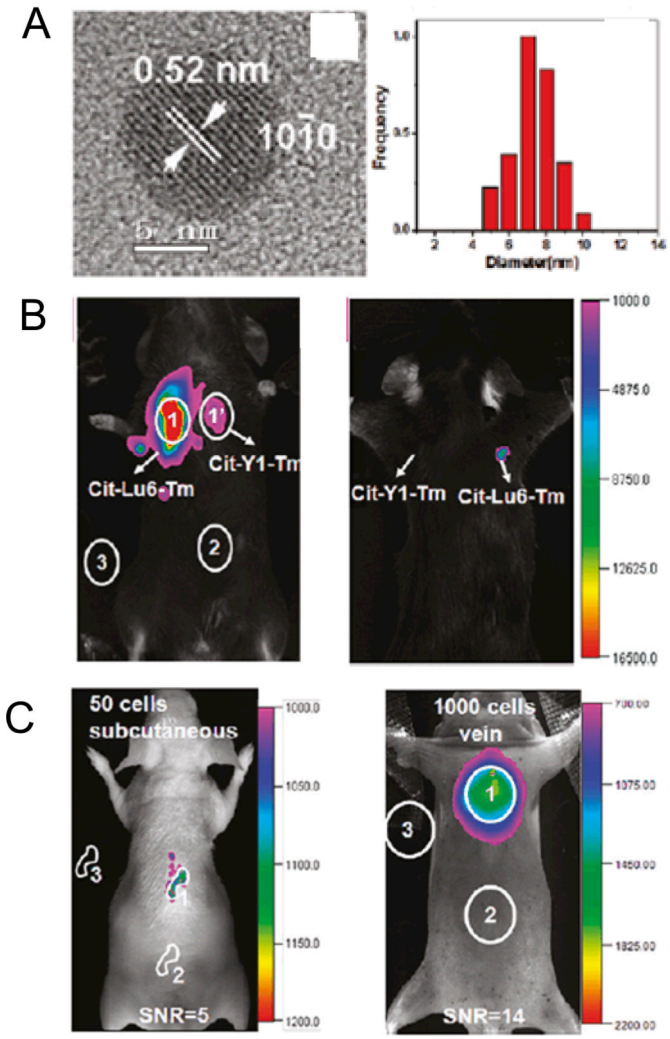

Fig. (2).

(A) A high resolution TEM (HR-TEM) image of ~8 nm sized β-$NaLuF_4$:Gd^{3+}/Yb^{3+}/Tm^{3+} (left) and a histogram of the particle size distribution (right). (B) *In vivo* imaging of a black mouse after subcutaneous injection of citric acid modified β-$NaLuF_4$:Gd^{3+}/Yb^{3+}/Tm^{3+} and citric acid modified β-$NaYF_4$:Yb^{3+}/Tm^{3+} when detected from the chest side (left) or the back side (right). (C) *In vivo* UCL imaging of athymic nude mice after subcutaneous injection of 50 KB cells (left) and intravenous injection of 1000 cells (right) after incubation with citric acid modified β-$NaLuF_4$:Gd^{3+}/Yb^{3+}/Tm^{3+} for 2 h. Reprinted with permission from [41].

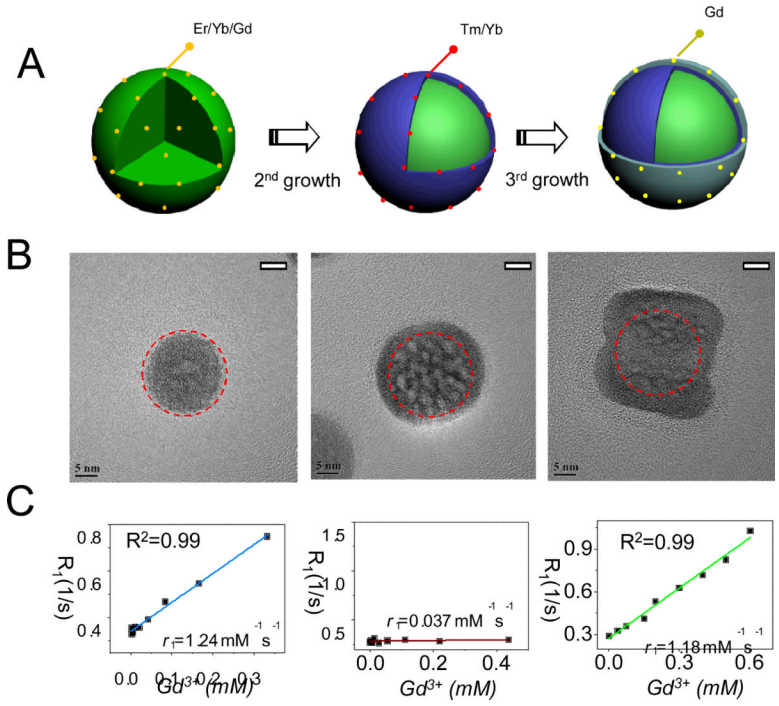

Fig. (3).

(A) A schematic illustration showing the synthesis of core@multi-shell UCNPs. (B) HR-TEM images of highly crystalline $NaYF_4$:Er^{3+}/Yb^{3+}/Gd^{3+} (1^{st}, left), $NaYF_4$:Er^{3+}/Yb^{3+}/Gd^{3+}@$NaYF_4$:Tm^{3+}/Yb^{3+} (1^{st}@2^{nd}, middle), $NaYF_4$:Er^{3+}/Yb^{3+}/Gd^{3+}@$NaYF_4$:Tm^{3+}/Yb^{3+}@$NaGdF_4$ (1^{st}@2^{nd}3@rd, right) nanoparticles. (C) Plots of longitudinal relaxation rate (R_1) *vs* Gd^{3+} concentration of three samples, (left) 1^{st}@SiO_2 (r_1=1.24 $mM^{-1}s^{-1}$), (middle) 1^{st}@2^{nd}@SiO_2 (r_1=0.037 $mM^{-1}s^{-1}$), and (right) 1^{st}@2^{nd}@3^{rd}@SiO_2 (r_1=1.18 $mM^{-1}s^{-1}$). Reprinted with permission from [46].

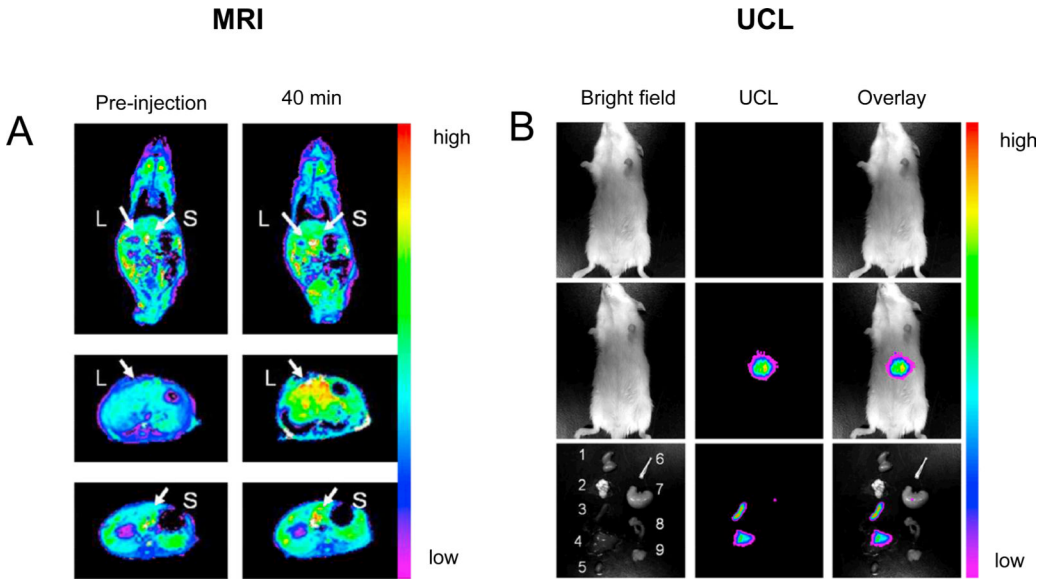

Fig. (4).

Magnetic resonance and upconversion luminescence imaging using carboxylic acid-functionalized $NaGdF_4$:Tm^{3+}/Er^{3+}/Yb^{3+} nanoparticles. (A) Color-mapped coronal MRI T_1-weighted images of the whole body (top) and transversal cross-sectional images of the liver (L, middle) and spleen (S, down) of mice before and 40 min after intravenous injection (dose: 1.5 mg/kg). (B) *In vivo* upconversion luminescence imaging of a mouse after intravenous injection without (top) and with (middle) carboxylic acid-functionalized $NaGdF_4$:Tm^{3+}/Er^{3+}/Yb^{3+} nanoparticles, (down) *ex vivo* UCL images. Reprinted with permission from [74].

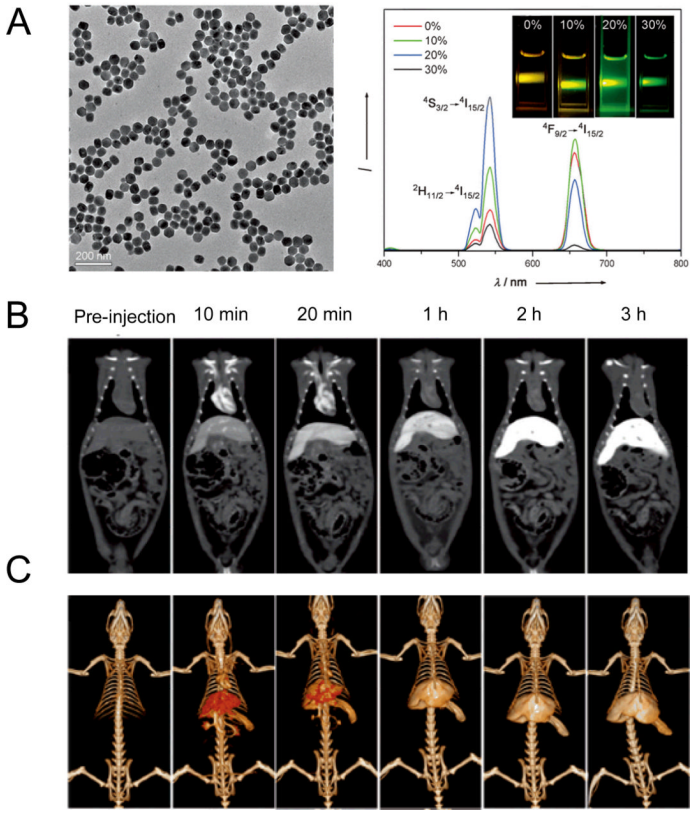

Fig. (5).

(A) Left: TEM image of PEG-$NaYbF_4$:Er^{3+}/Gd^{3+} dispersed in water. Right: room temperature NIR-to-Vis upconversion luminescence spectra of $NaYbF_4$:Er^{3+}/Gd^{3+} nanoparticles, the inset shows the upconversion luminescence photograph of the $NaYbF_4$:Er^{3+}/Gd^{3+} nanoparticles with different concentrations of Gd^{3+} under excitation at 980 nm. (B) *In vivo* CT coronal view images of a rat after intravenous injection of 1 mL PEG- $NaYbF_4$:Er^{3+}/Gd^{3+} (70 mg Yb/mL) solution at timed intervals. (C) The corresponding 3D renderings of *in vivo* CT images. Reprinted with permission from [51].

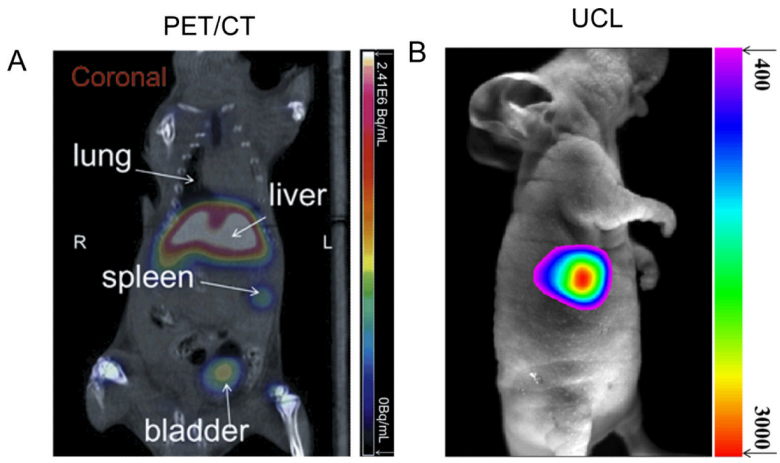

Fig. (6).
(A) PET/CT imaging of ^{18}F-labeled UCNP at 2 h after injection. (B) The *in vivo* UCL imaging result. Reprinted with permission from [89].

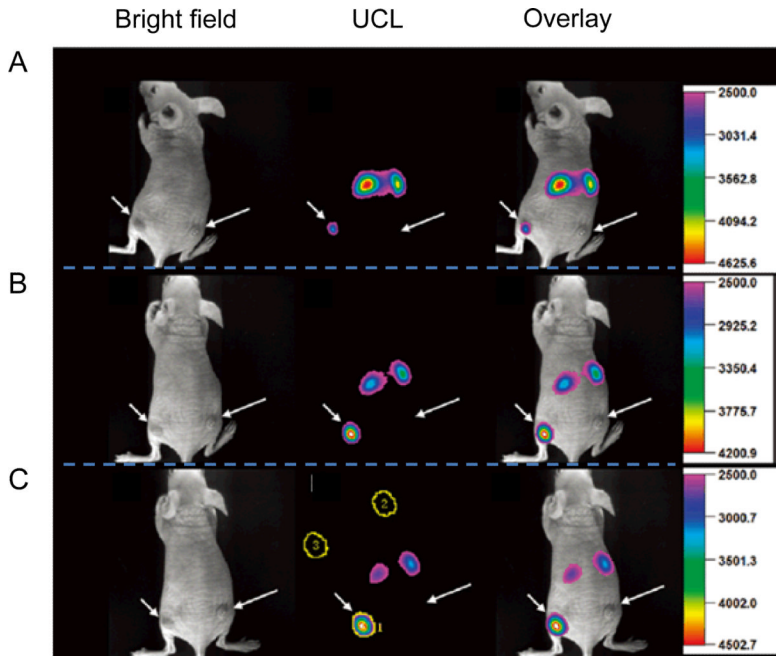

Fig. (7).

Time-dependent *in vivo* upconversion luminescence imaging of subcutaneous U87MG tumor (left hind leg, indicated by short arrows) and MCF-7 tumor (right hind leg, indicated by long arrows) borne by athymic nude mice after intravenous injection of UCNP-RGD over different time periods, (A) 1 h, (B) 4 h, and (C) 24 h. Reprinted with permission from [43].

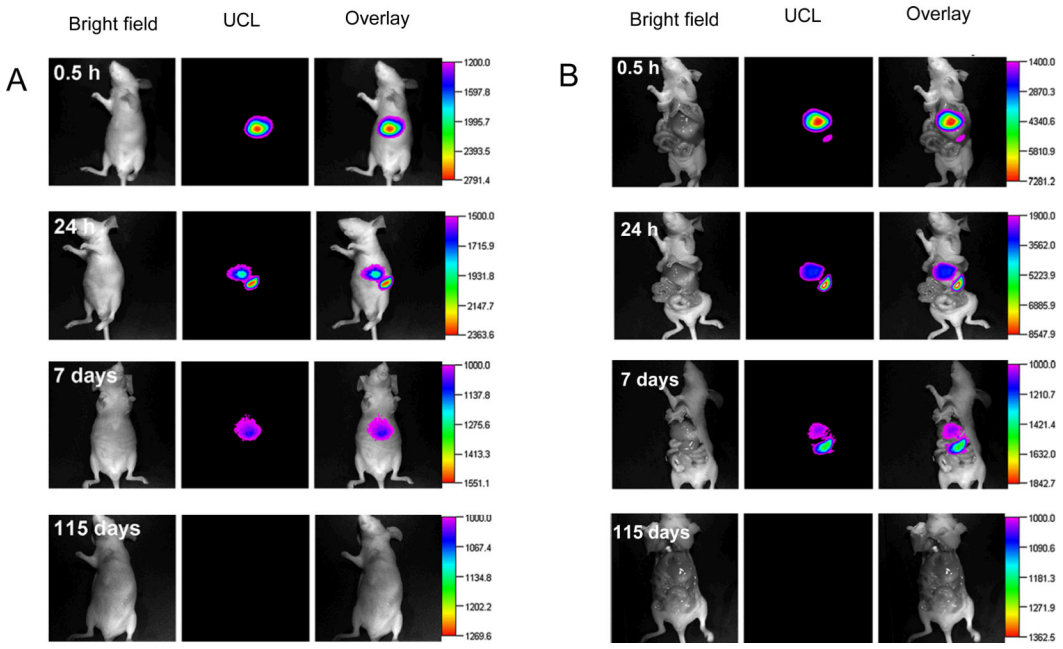

Fig. (8).

Real-time (A) *in vivo* and (B) *in situ* upconversion luminescence imaging of athymic nude mice after intravenous injection of PAA-UCNP (15 mg/kg) at different time points. Reprinted with permission from [49].

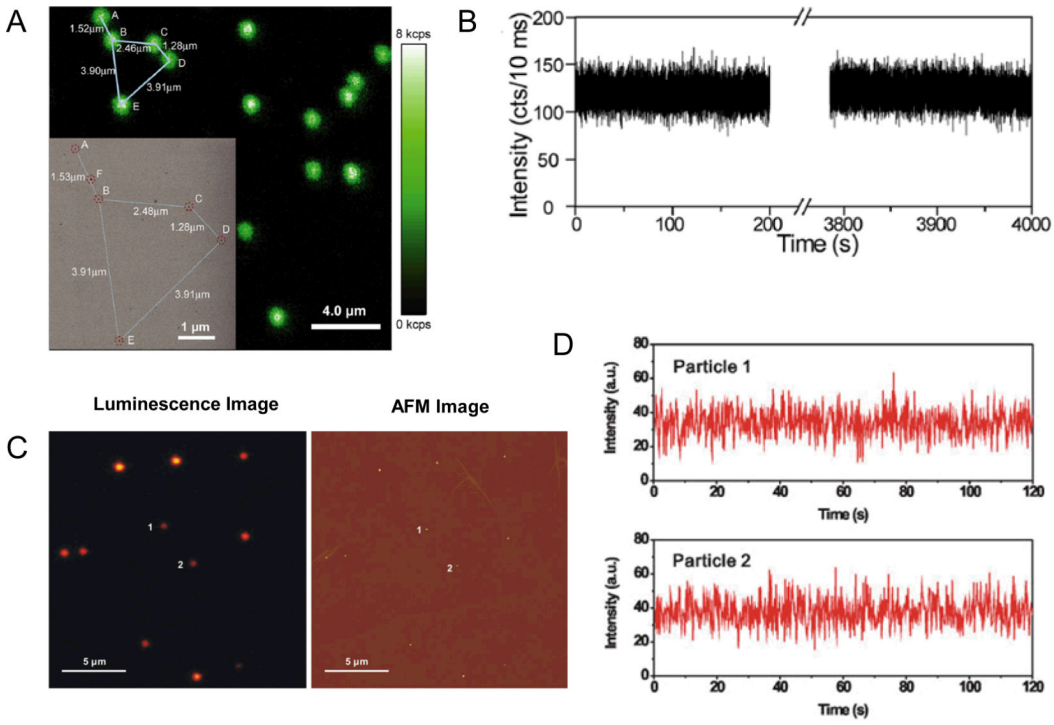

Fig. (9).

(A) Confocal upconverted luminescent image of individual UCNP. Insert shows the TM-SEM image taken at the upper left corner region of the optical image. (B) The time trace of emission intensity from a single UCNP under continuous laser illumination for over 1 h. (C) A luminescence image (left) and an AFM image (right) of UCNPs. (D) The luminescence time traces of the particles 1 and 2 acquired with 200 ms time bins. Reprinted with permission from [38, 40].

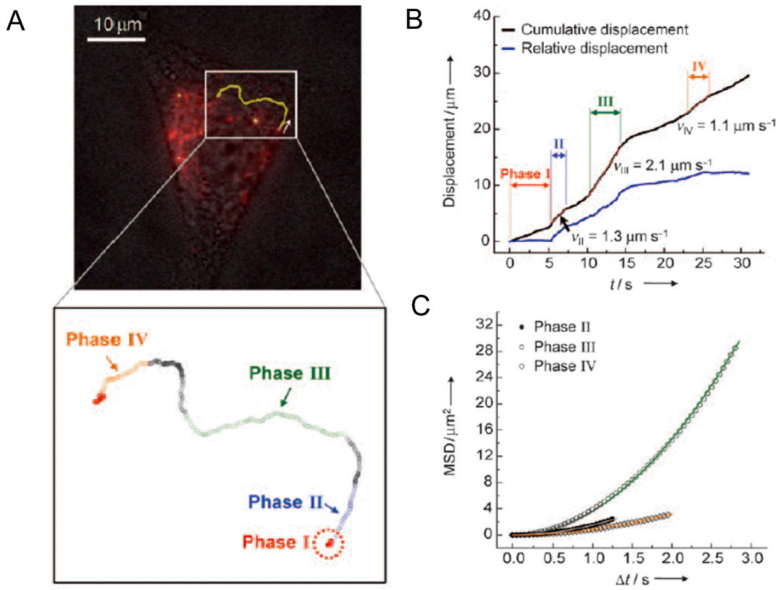

Fig. (10).

(A) Trajectory of a vesicle containing UCNPs transported from the cell periphery to the perinuclear region presumably by dyneins. (B) Cumulative and relative displacement traces for the trajectory shown in (A). (C) The mean square displacements (MSD) plots for phases II-IV. Reprinted with permission from [42].

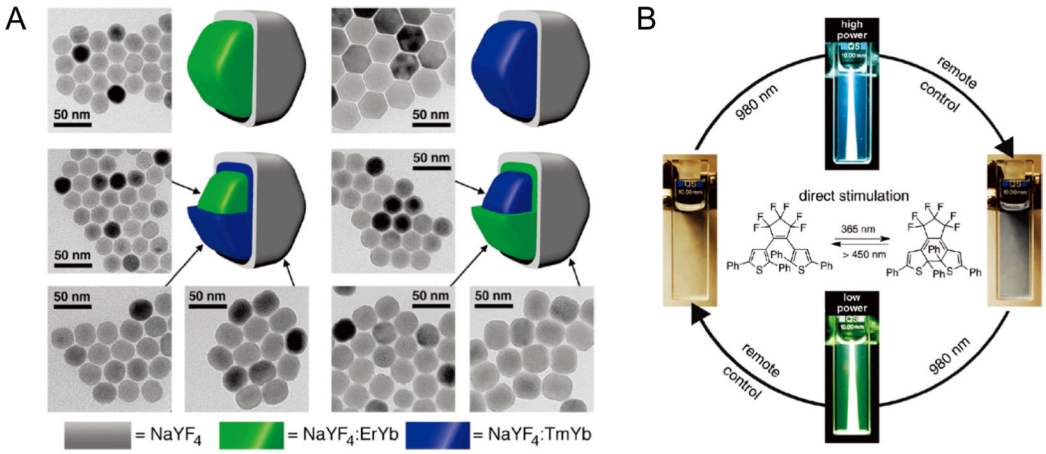

Fig. (11).

(A) TEM images of the core, core-shell, and core-shell-shell nanoparticles for $NaYF_4:Er^{3+}/Yb^{3+}@NaYF_4$ (**Er**), $NaYF_4:Tm^{3+}/Yb^{3+}@NaYF_4$ (**Tm**), $NaYF_4:Er^{3+}/Yb^{3+}@NaYF_4:Tm^{3+}/Yb3+@NaYF_4$ (**ErTm**), and $NaYF_4:Tm^{3+}/Yb^{3+}@NaYF_4:Er^{3+}/Yb^{3+}@NaYF_4$ (**TmEr**) UCNPs. (B) Bidirectional photoswitching of a THF (i.e. tetrahydrofuran) solution of DTE dispersed with **TmEr** core-shell-shell nanoparticles by varying only the intensity of the NIR light. Reprinted with permission from [124].

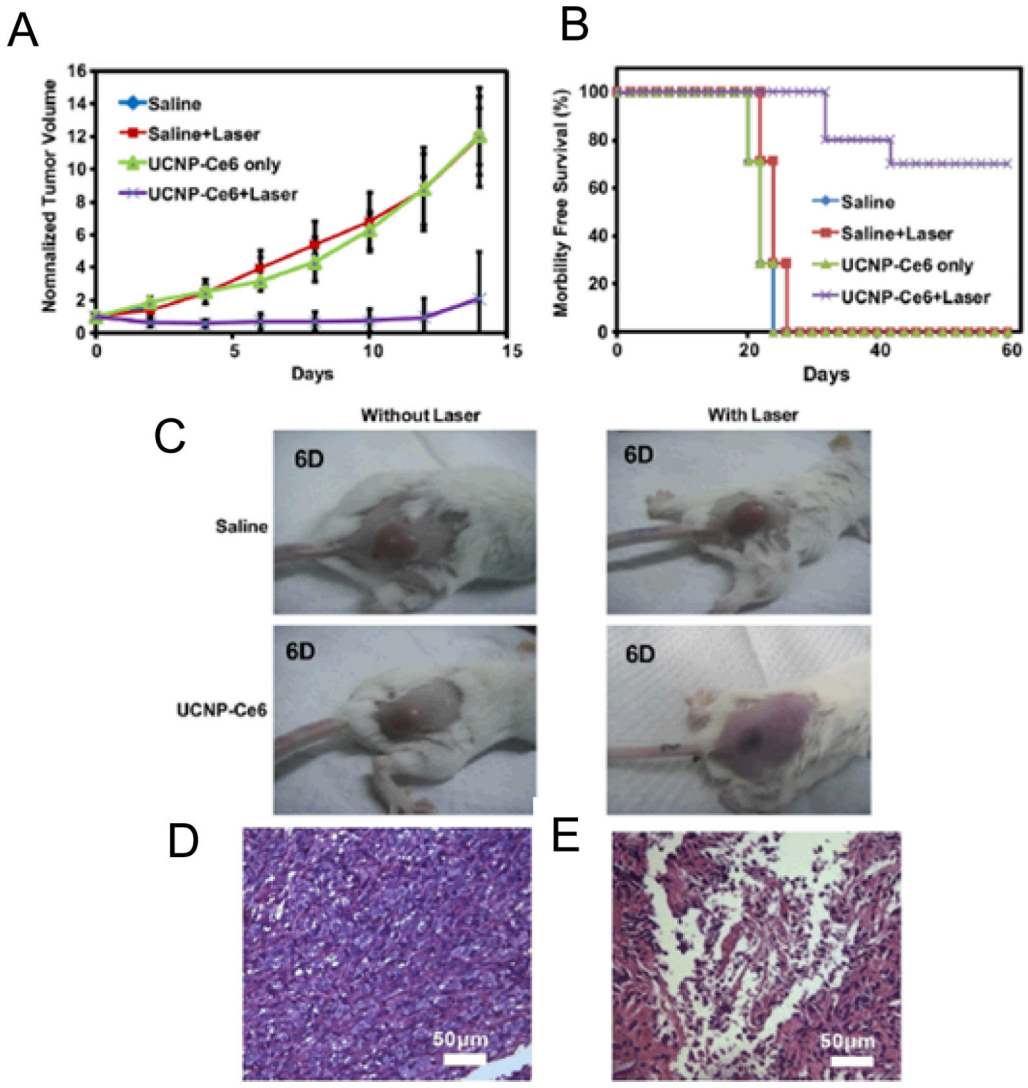

Fig. (12).

In vivo PDT treatment of tumor-bearing mice. (A) The growth of 4T1 tumors on different groups of mice after various treatments indicated. (B) The survival curves of mice in 60 days after various treatments indicated. (C) Representative photos of mice after various treatments indicated at the 6th day. Images of hematoxylin & eosin-stained tumor sections harvested from an untreated mouse (D) and a mouse 6 days after PDT treatment (E). Reprinted with permission from [132].

Table 1

f-UCNP for biological imaging and therapy *in vivo*

UCNPs or UCNP-based nanosystems	[a] Size (nm)	Surface modifications	*In vivo* imaging	*In vivo* therapy	Targeting strategy	References
$NaYF_4:Yb^{3+}/Tm^{3+}$	~50	PEI	UCL	-	-	[52]
$NaYF_4:Yb^{3+}/Er^{3+}@NaGdF_4$	24.0±2.3	Dense silica	UCL/MRI	-	-	[46]
$NaYF_4:Yb^{3+}/Er^{3+}@SiO_2@Fe_3O_4@SiO_2$	~20	Dense silica	UCL/MRI	-	-	[76]
$NaYF_4:Yb^{3+}/Er^{3+}@Fe_3O_4@Au$	~160	PAA+ Fe_3O_4+Au	UCL/MRI and lymph node mapping	-	-	[50]
$NaYF_4:Yb^{3+}/Tm^{3+}$	~30	PAA or PEG	UCL	-	-	[110]
$NaYF_4:Yb^{3+}/Tm^{3+}$ and $NaYF_4:Yb^{3+}/Er^{3+}$	~30	OA-PAA-PEG	UCL	-	-	[39]
$NaGdF_4:Yb^{3+}/Er^{3+}$	21.04±3.77	Ionic liquids	UCL/CT	-	-	[82]
$NaYF_4:Yb^{3+}/Tm^{3+}$	28±1	Mesoporous silica	UCL/MRI	-	-	[120]
$NaGdF_4:Yb^{3+}/Er^{3+}$ and $NaGdF_4:Yb^{3+}/Tm^{3+}$	~18	alphacyclodextrin (α-CD)+$^{18}F^-$	UCL/PET	-	-	[87]
$NaYF_4:Er^{3+}/Yb^{3+}$	10~20	Gd^{3+}+ aminocaproic acid+ folic acid+^{18}F	UCL/MRI/PET	-	-	[88]
$NaLuF_4:Gd^{3+}/Yb^{3+}/Tm^{3+}$	~8	Citric acid	UCL	-	-	[41]
$NaYbF_4:Er^{3+}/Gd^{3+}$	~20	DSPE-PEG2000	UCL/MRI/CT	-	-	[51]
$NaYF_4:Yb^{3+}/Tm^{3+}$	~20	3-mercaptopropionic acid	UCL	-	-	[73]
$NaYF_4:Yb^{3+}/Tm^{3+}$	~20	F127+$^{18}F^-$	UCL/PET and lymph node mapping	-	-	[89]
$NaGdF_4:Yb^{3+}/Er^{3+}/Mn^{2+}$	20~25	DSPE-PEG2000	UCL	-	-	[79]
$NaGdF_4:Yb^{3+}/Er^{3+}$	~30	PEG+Ce6	UCL	PDT	-	[132]
$NaYF_4:Yb^{3+}/Tm^{3+}@Fe_xO_y$	~30	dopamine	UCL/MRI and lymph node mapping	-	-	[77]
NaY/GdF_4: $Yb^{3+}/Er^{3+}/Tm^{3+}$	~25	Dense silica+Au	UCL/MRI/CT	-	-	[75]
$NaYF_4:Yb^{3+}/Tm^{3+}/Gd^{3+}$	~14	PEG+RGD	UCL	-	RGD-labeling	[43]
$NaYF_4:Yb^{3+}/Tm^{3+}$	~11.5	PAA	UCL	-	-	[49]
$NaYF_4:Er^{3+}/Yb^{3+}$	20×40	folic acid	UCL	-	FA-labeling	[105]
$Fe_3O_4@SiO_2@NaYF_4$: Er^{3+}/Yb^{3+}	~20±5	Porous silica	UCL/MRI	Chemotherapy	Magnetic targeting	[119]

UCNPs or UCNP-based nanosystems	**[a] Size (nm)**	**Surface modifications**	***In vivo* imaging**	***In vivo* therapy**	**Targeting strategy**	**References**
$NaGdF_4$: $Yb^{3+}/Er^{3+}/Tm^{3+}$	25~55	Azelaic acid	UCL/MRI	-	-	[74]
$NaYF_4$:$Er^{3+}/Yb^{3+}/Gd^{3+}$	22×19	Citric acid+$^{18}F^{-}$	UCL/MRI/PET	-	-	[90]
Fe_3O_4@$NaLuF_4$:$Yb^{3+}/Er^{3+}(Tm^{3+})$	~40	silica	UCL/MRI	-	-	[83]
$NaYF_4$:$Er^{3+}/Yb^{3+}/Ce^{3+}$	25×55	PEI+CTX	UCL	-	CTX-labeling	[106]
$NaYF_4$:Yb^{3+}/Tm^{3+} and $NaYF_4$:Yb^{3+}/Er^{3+}	~20	PEG	UCL lymph node imaging	-	-	[44]

[a] Here the size represents only the particles size (or the thickness) of UCNP.